Inverse Analysis of Experimental Scale Turbidity Currents by Deep Learning Neural Network

Zhirong Cai[1] and Hajime Naruse[1]

[1]Kyoto University

November 22, 2022

Abstract

Despite the importance of turbidity currents in environmental and resource geology, their flow conditions and mechanism are not well understood. To resolve this issue, a novel method for the inverse analysis of turbidity current using deep learning neural network (DNN) was proposed. This study aims to verify this method using artificial and flume experiment datasets. Development of inverse model by DNN involves two steps. First, artificial datasets of turbidites are produced using a forward model based on shallow water equation. To develop a inverse model, DNN then explores the functional relationship between initial flow conditions and characteristics of the turbidite deposit through the processing of artificial datasets. The developed inverse model was applied to 200 sets of artificial test data and four sets of experiment data. Results of inverse analysis of artificial test data indicated that the flow conditions can be precisely reconstructed from depositional characteristics of turbidites. For experimental turbidites, spatial distributions of grain size and thickness were accurately reconstructed. With regard to hydraulic conditions, reconstructed values of flow heights, sediment concentrations, and flow durations were close to the measured values. In contrast to the other values, there was a larger discrepancy between the measured and reconstructed values of flow velocity, which may be attributed to inaccuracies in sediment entrainment functions employed in the forward model.

Inverse Analysis of Experimental Scale Turbidity Currents by Deep Learning Neural Network

Zhirong Cai[1]*****, **Hajime Naruse**[1]

[1]Kyoto University

Key Points:

- A new method for inverse analysis of turbidity currents using deep learning neural network was performed on turbidity current deposits in experimental scale.
- Results of inverse analysis conducted for artificial datasets proved that flow conditions can be precisely reconstructed from depositional characteristics.
- Flow conditions and deposit profiles in flume experiments were also well reconstructed except for flow velocity.

*****Kyoto, Japan

Corresponding author: Zhirong Cai, `cai.zhirong.64w@kyoto-u.jp`

Abstract

Despite the importance of turbidity currents in environmental and resource geology, their flow conditions and mechanism are not well understood. To resolve this issue, a novel method for the inverse analysis of turbidity current using deep learning neural network (DNN) was proposed. This study aims to verify this method using artificial and flume experiment datasets. Development of inverse model by DNN involves two steps. First, artificial datasets of turbidites are produced using a forward model based on shallow water equation. To develop a inverse model, DNN then explores the functional relationship between initial flow conditions and characteristics of the turbidite deposit through the processing of artificial datasets. The developed inverse model was applied to 200 sets of artificial test data and four sets of experiment data. Results of inverse analysis of artificial test data indicated that the flow conditions can be precisely reconstructed from depositional characteristics of turbidites. For experimental turbidites, spatial distributions of grain size and thickness were accurately reconstructed. With regard to hydraulic conditions, reconstructed values of flow heights, sediment concentrations, and flow durations were close to the measured values. In contrast to the other values, there was a larger discrepancy between the measured and reconstructed values of flow velocity, which may be attributed to inaccuracies in sediment entrainment functions employed in the forward model.

1 Introduction

A turbidity current is a process of sediment transport into subaqueous environments such as deep lakes and ocean (Daly, 1936; Johnson, 1939). The deposits of turbidity currents are called turbidites, which are often characterized by graded bedding and sedimentary succession called the Bouma sequence (e.g., Kuenen & Migliorini, 1950; Bouma, 1962; Talling et al., 2012). Turbidite deposits have been an active area of study because of their close association with petroleum resources and their role in the destruction of sea-floor equipment, such as the submarine cables (Weimer & Slatt, 2007; Talling et al., 2015). Furthermore, turbidites are often deposited as a result of tsunami triggered turbidity currents (Arai et al., 2013),and thus are potentially useful for estimating the recurrence intervals of geohazards.

To understand the characteristics of turbidites and their implications, it is essential to study the flow behavior of turbidity currents (Talling et al., 2007). However, knowledge in this area remains limited because of difficulties in the direct observation of turbidity currents. A few in-situ measurements have been made (e.g., Xu et al., 2004; Vangriesheim et al., 2009; Arai et al., 2013; Paull et al., 2018), but hydraulic conditions measured, such as sediment concentration and flow velocity, were unclear because of the destructive nature and unpredictable occurrences of turbidity currents (Naruse & Olariu, 2008; Falcini et al., 2009; Lesshafft & Marquet, 2010; Talling et al., 2015). Therefore, inverse analysis that reconstructs the flow conditions of turbidity currents from their deposits is crucial for estimating the flow conditions in natural environments.

Prior to this research, inverse analysis of turbidity currents was conducted by Baas et al. (2000), where flow velocity was reconstructed through analyses of sedimentary structures of turbidites. The results gave an estimation of the hydraulic conditions of flow at a single location, but did not provide a reconstruction of spatial evolution of the turbidity current. By contrast, inverse analysis methods in previous studies based on numerical models provided more detailed insights to the spatial structure of flow and the evolution of flow over time (e.g., Falcini et al., 2009; Lesshafft & Marquet, 2010; Parkinson et al., 2017). However, the method proposed by Falcini et al. (2009) assumed steady flow conditions and was simplified for obtaining analytical solutions, preventing it from accurately illustrating the flow mechanism of unsteady turbidity currents that can produce normally graded bedding. Consequently, this method can not be applied to normally graded beds, which are typical characteristics of turbidites. Other studies employed the optimization method estimated the hydraulic parameters through optimizing the input parameters of numerical models, so that the resulting calculations fit the observed data from turbidites (Lesshafft & Marquet, 2010). This method can provide a relatively good reconstruction of the hydraulic conditions of turbidity currents, but has extremely heavy calculation load. Therefore, it is impossible to apply the method to natural scale turbidites, which typically run over tens to hundreds of kilometers and flow continuously for several hours (Talling et al., 2015). Optimization using the adjoint approach proposed by Parkinson et al. (2017) solved the problem of heavy calculation load, but the reconstructed values were very low in accuracy.

To resolve the aforementioned issues, Naruse and Nakao (2017) developed a new method for inverse analysis of turbidite deposits using deep learning neural network (DNN). DNN is a computational scheme that works as a universal function approximator (Liang & Srikant, 2016). Previously, it was applied to problems such as landslide susceptibility analyses (Pradhan et al., 2010) and identification of lithology from well log data (Rogers et al., 1992), where the empirical relationship between the observed data and the parameters aimed to be predicted were explored. In case of turbidity currents, however, it is impossible to obtain sufficient datasets of in-situ measurements of flow characteristics for developing a DNN inverse model. Thus, Naruse and Nakao

(2017) produced artificial datasets of turbidites using a numerical model. The produced datasets were inputted into DNN to explore the functional relationship between the deposits and the initial flow conditions. After this process, which is referred to as training, DNN becomes capable of making estimations of flow conditions from new turbidite data. Although it was proven by Naruse and Nakao (2017) that DNN is capable of reconstructing flow properties from artificial test datasets, it has yet to be tested with actual turbidite data.

In this study, we verified the ability of DNN to perform inverse analysis of turbidity currents by applying DNN to data collected from actual turbidites deposited in flume experiments. During each flume experiment, a turbidity current was generated under a controlled environment. Conditions including flow duration and initial hydraulic conditions can be set manually, and measurements of these parameters can also be conducted easily during the flow. Thus, rather than data measured in nature, data collected from flume experiment works better as a first step to verify the accuracy of DNN for inverse analysis of turbidity currents.

Here, we implemented the forward model and DNN for inverse analysis. Trained DNN was first tested with artificial data of experimental scale turbidity currents. Then, trained DNN was tested with flume experiment data. Initial flow conditions of experiments were reconstructed from deposit profiles sampled. These values of flow conditions were then fed into the forward model to reconstruct the spatio-temporal evolution of the flow. Reconsturcted hydraulic conditions during the flow and the eventual grain size distribution of the deposits were compared with the measured values.

2 Forward Model

2.1 Governing Equations

The forward model implemented in this study is a layer-averaged model based on Kostic and Parker (2006). It is expanded to account for the transport and deposition of non-uniform grain size distribution discretized to multiple grain-size classes in Nakao and Naruse (2017) (Figure 1). The five governing equations are as follows:

$$\frac{\partial H}{\partial t} + U\frac{\partial H}{\partial x} = e_{\mathrm{w}}U - H\frac{\partial U}{\partial x}, \tag{1}$$

$$\frac{\partial U}{\partial t} + U\frac{\partial U}{\partial x} = RC_{\mathrm{T}}g(S - \frac{\partial H}{\partial x}) - \frac{1}{2}gHR\frac{\partial C_{\mathrm{T}}}{\partial x} - \frac{U^2}{H}(c_{\mathrm{f}} - e_{\mathrm{w}}), \tag{2}$$

$$\frac{\partial C_i}{\partial t} + U\frac{\partial C_i}{\partial x} = \frac{w_i}{H}(F_i e_{\mathrm{s}i} - r_{\mathrm{o}}C_i) - \frac{e_{\mathrm{w}}C_iU}{H}, \tag{3}$$

$$\frac{\partial \eta_i}{\partial t} = \frac{w_i}{1 - \lambda_{\mathrm{p}}}(r_{\mathrm{o}}C_i - e_{\mathrm{s}i}F_i), \tag{4}$$

$$\frac{\partial F_i}{\partial t} + \frac{F_i}{L_{\mathrm{a}}}\frac{\partial \eta_{\mathrm{T}}}{\partial t} = \frac{w_i}{L_{\mathrm{a}}(1 - \lambda_{\mathrm{p}})}(r_{\mathrm{o}}C_i - e_{\mathrm{s}i}F_i), \tag{5}$$

where the equations represent fluid mass conservation (equation 1), momentum conservation (equation 2), sediment mass conservation (equation 3), mass conservation in bed (Exner's equation) (equation 4) and sediment mass conservation in active layer (equation 5) (Nakao & Naruse, 2017).

Let x and t be the bed-attached streamwise coordinate and time, respectively. Parameters H, U and C_i are the flow height, the layer-averaged velocity and the layer-averaged volumetric concentration of suspended sediment of the ith grain-size class, respectively. In this study, the number of grain-size classes and representative grain diameters were determined based on the grain size distribution of experiments performed (specific values noted in Section 5.1). Parameter C_{T} denotes the layer-averaged total

124 concentration of suspended sediment ($C_T = \sum C_i$), and g is gravitational acceleration.
125 Parameters S and c_f are the slope gradient and the friction coefficient, respectively.
126 Sediment properties are described by R, the submerged specific density of sediment;
127 w_i, the settling velocity of a sediment particle of the ith grain-size class; and λ_p, the
128 porosity of bed sediment. Parameter η_i is the volume per unit area of bed sediment
129 of the ith grain-size class and η_T is the sum of all η_i ($\eta_T = \sum \eta_i$). Parameters L_a, the
130 active layer thickness, and F_i, the volume fraction of the ith grain-size class in active
131 layer, describe the structure of active layer. Parameters e_{si}, e_w and r_o are the entrain-
132 ment rate of sediment of the ith grain-size class into suspension, the entrainment rate
133 of ambient water to flow, and the ratio of near-bed suspended sediment concentration
134 to the layer-averaged concentration of suspended sediment, respectively (Figure 1).
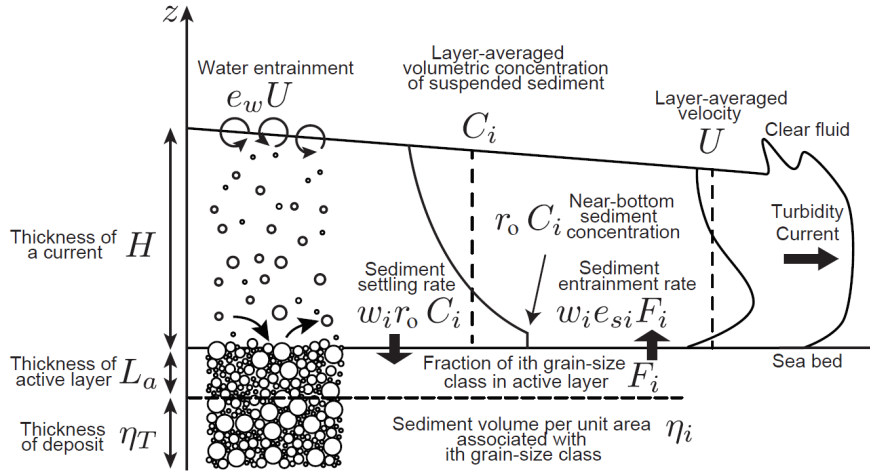135 Closure equations of the parameters mentioned are described in Section 2.2.

Figure 1. Schematic diagram of processes considered in the forward model from Nakao and Naruse (2017).

2.2 Closure Equations

137 Empirical formulations from previous studies are adapted to close the govern-
138 ing equations. In this study, the friction coefficient c_f is assumed to be a constant
139 value. The particle settling velocity w_i for each grain-size class with a representative
140 grain diameter D_i is calculated using the relation from Dietrich (1982), which can be
141 expressed as follows:

$$w_i = R_{fi}\sqrt{RgD_i}, \tag{6}$$
$$R_{fi} = \exp(-b_1 + b_2\log(Re_{pi}) - b_3(\log(Re_{pi}))^2 - b_4(\log(Re_{pi}))^3 + b_5(\log(Re_{pi}))^4), \tag{7}$$
$$Re_{pi} = \frac{\sqrt{RgD_i}D_i}{\nu}, \tag{8}$$

142 where b_1, b_2, b_3, b_4 and b_5 are 2.891394, 0.95296, 0.056835, 0,000245 and 0.000245,
143 respectively. e_w is calculated using the empirical formula from Fukushima et al. (1985)
144 as follows:

$$e_w = \frac{0.00153}{0.0204 + (RC_T H/U^2)}. \tag{9}$$

The entrainment coefficient of sediment e_s is calculated using the empirical relation from Wright and Parker (2004):

$$e_{si} = \frac{aZ^5}{1 + (a/0.03)Z^5},\tag{10}$$

$$Z = \alpha_1 \frac{u_*}{w_i} Re_p^{\alpha_2} S_f^{0.08},\tag{11}$$

where shear velocity u_* and friction slope S_f are calculated as follows:

$$u_* = \sqrt{c_f}U,\tag{12}$$

$$S_f = \frac{c_f U^2}{RgC_T H},\tag{13}$$

and the constants α_1 and α_2 are 0.586 and 1.23 respectively if $Re_p \leq 2.36$. If $Re_p > 2.36$, then α_1 and α_2 are 1.0 and 0.6, respectively. Kinematic viscosity of water ν is calculated as follows:

$$\nu = \mu/\rho,\tag{14}$$

where ρ and μ denote the density of water and the dynamic viscosity of water, respectively. Experimentally determined values for μ at 20.0 °C (Rumble, 2018) were used in the calculation of ν in this study.

2.3 Implementation of Forward Model

In this study, the constrained interpolation profile (CIP) method (Yabe et al., 2001) was used for the integration of the partial differential equations 1, 2, and 3. To stabilize the calculation, artificial viscosity was applied with the scheme of Jameson et al. (1981), in which the parameter κ was set to 0.25. The two-step Adams-Bashforth method was used to solve ordinary differential equations 4 and 5. Interval of spatial grids Δx was set to 0.05 m and time step Δt was set to 0.01 s. Initial values of S were 10% for all grids.

Dirichlet boundary condition was used for the upstream boundary, in which all flow parameters at the upper boundary of calculation domain, including the initial flow height H_0, the initial flow velocity U_0, the initial total volumetric concentration of sediment $C_{T,0}$, and the initial volumetric concentration of each grain-size class $C_{i,0}$, were set to be constant. Parameter $F_{i,0}$, the initial volume fraction of the ith grain-size class in active layer, was set to 0.25 for all grain-size classes. The downstream boundary was the Neumann boundary condition where all parameters were set to the same values as those of the grid adjacent to the lower boundary toward the upstream direction. Other than the upstream boundary, all flow parameters, except the flow height H, were initialized to zero. H was initialized to 0.0001.

Properties of fluids and sediment particles were set as follows. Density of fluid ρ were set to be 1000.0 kg/m³, and submerged specific density of sediment $R = (\rho_s - \rho)/\rho$ was set differently according to the types of particles used in experiments (rho_s is the density of sediment particles), which are stated in Section 4.1. The porosity of bed sediment λ_p was assumed to be 0.4. In this study, both the friction coefficient c_f and ratio of near-bed concentration to layer-averaged values r_o were assumed to be constant, which were set to 0.002 and 1.5 (Kostic & Parker, 2006). Also, the thickness of the active layer L_a was set to be constant (0.003 m). The gravitational acceleration g was 9.81 m/s².

3 Inverse Analysis by Deep Learning Neural Network

In this method, initial flow conditions of turbidity currents are reconstructed from its turbidite deposits. DNN first explores the functional relationship between the

initial flow conditions of turbidity currents and the resulting turbidite deposits in a process called training. After the training process, DNN is applied to new turbidite datasets for inverse analysis. In preparation for training, artificial training datasets are produced using the forward model. During the training process, training datasets are fed into DNN. DNN examines the datasets and adjusts to make good estimation of the initial flow conditions from the deposit profile. After training, DNN, which is now capable of predicting the initial flow conditions of new turbidites based on the functional relationship it discovered, is tested with independent artificial datasets that are also produced from the forward model and with flume experiment data.

3.1 Production of Training Data

A training dataset is a combination of randomly generated initial flow conditions at the upstream boundary of the flow and a matching deposit profile calculated by the forward model. A program in Python was written to generate sets of initial flow conditions. Each set of flow conditions generated consists of an initial flow velocity U_0, an initial flow height H_0, a flow duration T_d, and the initial concentrations of each grain-size class $C_{i,0}$. Other variables, such as slope, are set to constant values.

The forward model calculates the deposit profile of a turbidite using the randomly generated initial flow conditions. The deposit profile is calculated as volume per unit area for each grain-size class at a total of 80 locations within a 4 m range. Each data point is 0.05 m away from its neighboring points. The ranges of randomly generated initial flow conditions are shown in Table 1. In this study, 11800 training datasets were used for training and 200 datasets were used for verification of DNN. The test artificial datasets for verification were produced independently from the training datasets.

Table 1. Range of initial flow conditions generated for the production of training datasets.

Parameter	Minimum	Maximum
H_0 (m)	0.005	0.3
U_0 (m/s)	0.001	0.3
$C_{i,0}$	0.0001	0.02
T_d (s)	1080	120

3.2 Structure of Deep Learning Neural Network

The type of neural network used in this study is the fully connected neural network, which consists of an input layer, several hidden layers, and an output layer. Each layer consists of a number of nodes. Each node connects with every node in the adjacent layers (Figure 2A). In the input layer, the nodes hold values of the deposit profile, i.e. the volume-per-unit-area for all grain-size classes at spatial grids. In the output layer, the nodes hold estimates of the parameters we seek to reconstruct, which in this case are the initial flow conditions U_0, H_0, $C_{i,0}$ and the flow duration T_d. The activation function used in this study is ReLU, which is one of the most commonly used activation functions for DNN and is proven to perform calculations at a higher speed than other activation functions (Krizhevsky et al., 2012).

Before training, the weight coefficients are set to random values. As the training process begins, the values of deposit profile from the training datasets are fed into the input layer. These values propagate through the hidden layers of DNN and estimates of initial flow conditions are outputted at the output layer. At this point of training, DNN
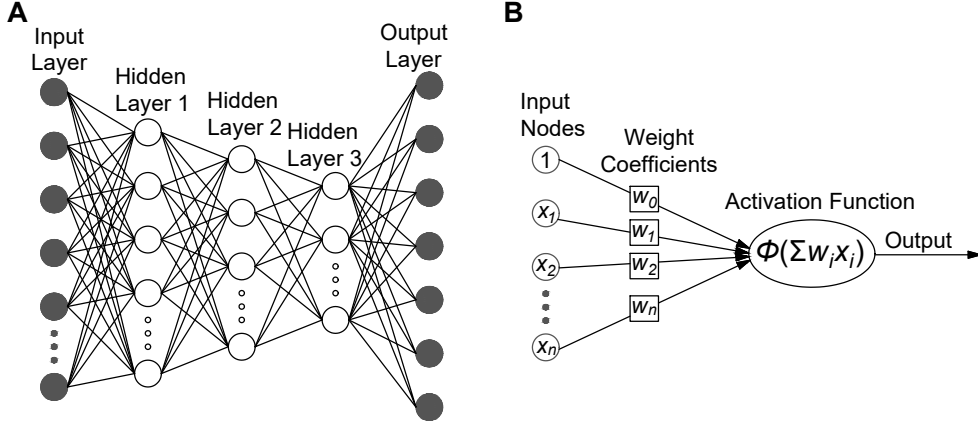
Figure 2. Schematic diagrams of DNN. A. Overall structure of DNN. B. Concept of weight coefficient and activation function.

is yet to adapt its internal variables to the functional relationship between turbidite deposits and initial flow conditions, thus the initial estimates are expected to be largely off from the actual values. To explore this functional relationship, a loss function is used to evaluate the accuracy of the estimated values. The loss function used in this case is the mean squared error function, which is considered as one of the best functions for regression (Wang & Bovik, 2009). The gradient of the loss function is calculated and fed back to the hidden layers of DNN through a process called backpropagation (Nielsen, 2015; Schmidhuber, 2015), where the internal values of DNN are optimized toward minimizing the difference between the estimated and actual values. This process is repeated for every epoch of calculation. An epoch is a cycle of calculation in DNN that involves one forward pass and one backpropagation of all training data.

The optimization algorithm used in this study is stochastic gradient descent (SGD), which drastically reduces the amount of calculation involved in training without compromising accuracy relative to previous algorithms of gradient descent (Bottou, 2010). In this study, Nesterov momentum is employed with SGD (Ruder, 2016). Because of difference in the order of the range of initial flow conditions, normalization needs to be applied to training datasets before they are inputted to DNN. In this case, all values are normalized to be between 0 and 1 for DNN to consider all parameters at equal weights. The hyperparameters including the number of layers, number of nodes at each layer, dropout rate, validation split, learning rate, batch size, epoch, and momentum were adjusted manually. Various combinations were attempted and the best combination of hyperparameters was chosen based on the performance of DNN, which is judged on the basis of the final validation loss.

In this study, DNN was programmed in Python using the package Keras 2.2.4. The package Tensorflow 1.14.0 (Abadi et al., 2015) was used for backend calculation. Calculations were conducted using GPU NVIDIA GeForce GTX 1080 Ti.

3.3 Evaluation of Trained DNN Model

During the verification of DNN with test artificial datasets (Section 5.1), reconstruction result of each parameter was evaluated using bias (B) and sample standard deviation (s) of residuals. The calculations were conducted using the following equa-

253 tions:

$$B = \frac{\sum x_i}{n}, \tag{15}$$

$$s = \sqrt{\frac{\sum (x_i - B)^2}{n - 1}}, \tag{16}$$

254 where n is the number of test datasets, and x_i denotes the residual of the specific recon-
255 structed parameter for the ith test dataset. The calculated s and B for reconstructed
256 parameters are listed in Table 4 and Table 5. The value of s for each reconstructed
257 parameter was compared with a representative value C_v^*, which is the mid-value over
258 the range in which the specific parameter was generated (Table 1). The confidence
259 interval of B was determined using bootstrap resampling method (Davison & Hink-
260 ley, 1997). Resampling of B was conducted for 10000 times and the 95% confidence
261 interval (CI) of B was determined.

262 During the verification of DNN using flume experiment data (Section 5.2), flow
263 parameters at the upstream end of simulation were reconstructed from the measured
264 properties of the deposit profile. The upstream end of simulation was set at 1.0 m
265 from the upstream boundary of the flume. The reconstructed parameters were in-
266 putted into the forward model so that the flow parameters downstream and the time
267 evolution of deposit profile were calculated. The calculated flow parameters down-
268 stream were compared with the flow conditions measured during experiments. The
269 deposit profile calculated from the reconstructed flow parameters was also compared
270 with the measured deposit profile that was used for inversion.

4 Flume Experiments

4.1 Experiment Settings

273 In this study, flume experiments were conducted using a flume located in the
274 basement of Building No.1 of the Faculty of Science at Yoshida Campus, Kyoto Uni-
275 versity. The flume was made of acrylic panels and is 4 m in length, 0.12 m in width
276 and 0.5 m in depth. It was submerged in a tank made of glass panels and steel sup-
277 porting frame. The tank was 5.5 m in length, 2.5 m in width and 1.8 m in depth.
278 Slope of channel floor changes at a middle point of the flume (1.0 m from the inlet),
279 where the upstream slope a was set to 26.8% and the downstream slope b was set
280 to 10% (Figure 3). Sediment was mixed with water in two mixing tanks before the
281 experiments.

282 During the experiments, the mixture of sediment and water was first pumped to
283 the constant head tank and then released into the flume from a valve at the base of
284 the constant head tank. Flow discharge was regulated through adjusting the degree
285 of opening of the valve. The amount of mixture in the constant head tank was kept
286 at a constant level to maintain a stable flow discharge. The damping tank at the
287 downstream end of the flume prevented flow from reflecting back toward the upstream
288 side. A pipe of freshwater supply was placed at the top of the damping tank, and
289 a draining pipe was placed at the bottom of the damping tank. The combination of
290 these two pipes kept the level of water in the tank constant and prevented reflection
291 of flow.

292 Four experiments were conducted in this study. Two experiments were performed
293 using two types of plastic particle (experiments PP1, PP2 (Section 4.3)). One of the
294 types of plastic particle used, polyvinyl chloride, had a density of 1.45 g/cm^3 and
295 an average grain diameter of 0.120 mm. The other type of plastic particle used,
296 melamine, had a density of 1.45 g/cm^3 and an average grain diameter of 0.220 mm.
297 Two experiments were performed using a mixture of siliciclastic sand and polyvinyl
298 chloride plastic particle (experiments BS1, BS2 (Section 4.3)). Siliciclastic sand had

a density of 2.65 g/cm^3 and an average grain diameter of 0.250 mm. The submerged specific gravity R of the plastic particles was 0.45, whereas that of the siliciclastic sand was 1.65.

4.2 Measurements and Data Analysis

Before each experiment, tank water temperature was measured using a glass alcohol thermometer. A beaker of the mixture in tank was sampled to measure the initial concentration in tank. Flow velocity during experiment was measured with an acoustic Doppler velocity profiler (ADVP; Nortek Vectrino Profiler). The functional range of the ADVP used was $4.0 - 7.0$ cm from the probe. To obtain the vertical velocity profile of the flow, an actuator was used to adjust the position of the ADVP during experiments.

A siphon with 10 plastic tubes was used to measure the suspended sediment concentration of flow. The tubes were aligned vertically at 1.0 cm intervals and were positioned such that samples were collected at 0.0 to 9.0 cm above bed. Aluminum tubes with an outer diameter of 8.0 mm and an inner diameter of 5.0 mm were attached to the outlets of the plastic tubes to stabilize its position. Sampling using siphon was conducted when the flow reached a quasi-equilibrium state. The state of flow was determined by observation of the development of flow. Two single-lens reflex cameras were used to record the experiments. Flow height was determined based on the video recorded.

After the experiments, the flume was left untouched for 1 to 3 days for the suspended sediment to settle. Afterward, photos were taken from a lateral view perpendicular to the flume. The lateral view of the deposited sediment could be seen together with a ruler in the photos. The height of deposit was determined from the photos. Water was then drained slowly from the tank with a bath pump at a rate of 0.0002333 m^3/s. After water was drained, deposited sediment was sampled at 20 cm intervals starting from the upstream boundary of the flume.

Samples from the siphon and tank were first weighed right after they were collected. Following the weighing, samples from the deposited sediment and from siphon and tank were dried. Samples from the siphon and tank were weighed again after drying, and the measurements were recorded for calculation of the sediment concentration in flow and in tank. Grain size distribution analysis was conducted in a settling tube for all sediment samples. The settling tube used was 1.8 m long. Calculation of grain size distribution was performed using STube (Naruse, 2005). Particle settling velocity was calculated using Gibbs (1974).

The measured grain-size distribution of sediment was discretized to four grain-size classes. For experiments using plastic particle only, representative grain diameter of grain-size classes 1, 2, 3 and 4 were set to be 210 μm, 149 μm, 105 μm and 74.3 μm, respectively. For experiments using a mixture of siliciclastic sand and plastic particle, representative grain diameter of grain-size classes 1, 2, 3 and 4 were set to be 297 μm, 210 μm, 149 μm and 105 μm, respectively. Grain size distributions of sand and plastic particle partially overlaps, thus concentrations of grain-size classes 2 and 3 were each represented by two separate parameters, i.e. $C_{2,\mathrm{BS},0}$ and $C_{2,\mathrm{PP},0}$, $C_{3,\mathrm{BS},0}$ and $C_{3,\mathrm{PP},0}$, respectively. BS and PP represents the siliciclastic sand and the plastic particle portions, respectively, of the grain-size classes 2 and 3.

In steady flow conditions, the relationship between the layer-averaged flow velocity U, the layer-averaged sediment volumetric concentration C, and the flow height H is defined as follows (Garcia & Parker, 1993):

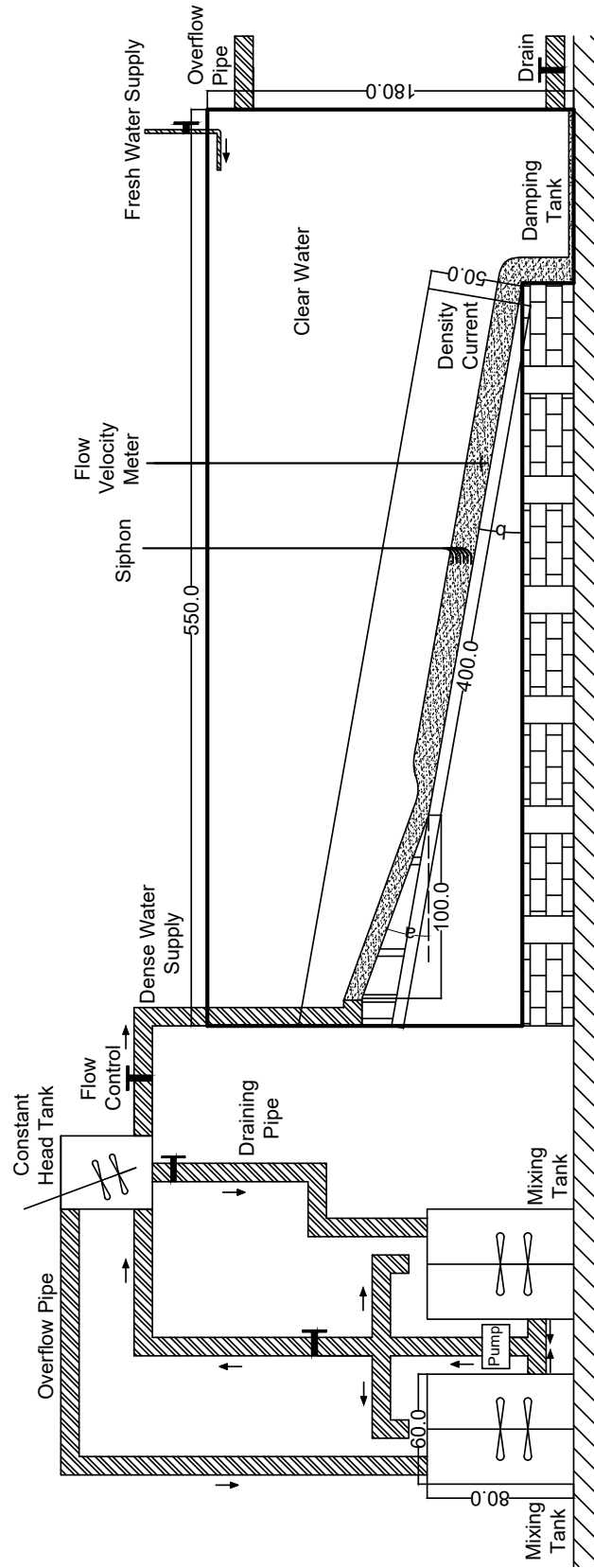$$UCH \quad = \quad \int_a^\infty u_z c_z dz, \tag{17}$$

Figure 3. Schematic diagram of flume used for experiment. (All values have unit cm.)

where u_z and c_z are the flow velocity and sediment volumetric concentration, respectively, at elevation z above bed. The relationship between the layer-averaged flow velocity U and the velocity maximum U_m is defined with the following equation (Altinakar et al., 1996):

$$\frac{U_m}{U} = 1.3. \tag{18}$$

The layer-averaged flow velocity was calculated from the velocity profile measured by the ADVP using the relationship described by equation 18. The sediment volumetric concentration was calculated from siphon measurements using the relationship described by equation 17.

4.3 Experimental Conditions

The experimental conditions for the four runs conducted are outlined in Table 2 and Table 3. C_{TT} is the total concentration of sediment in the mixing tank. C_{1T}, C_{2T}, C_{3T}, C_{4T} are the concentrations of grain-size classes 1, 2, 3, and 4, respectively. $C_{2T,BS}$ and $C_{2T,PP}$, $C_{3T,BS}$ and $C_{3T,PP}$ in Table 3 are concentrations of the siliciclastic sand portion and plastic particle portion, respectively, of grain-size classes 2 and 3. Parameter x_C is the position of siphon downstream, whereas x_U is the position of flow velocity meter downstream. x_H is the position where flow height was measured from video taken. Temperature is the measured temperature of clear water in tank before experiment.

Table 2. Conditions and settings of experiments conducted with two types of plastic particle.

	PP1	PP2
C_{TT}	0.0191	0.0276
C_{1T}	0.0102	0.0160
C_{2T}	0.00713	0.00820
C_{3T}	0.00146	0.00254
C_{4T}	0.000366	0.000817
x_C (m)	1.08	2.10
x_U (m)	1.46	2.48
x_H (m)	1.10	1.10
Temperature (°C)	22.5	17.0

5 Results

Inverse analysis was applied to deposits within a 2.6 m range downstream starting at the end of slope a (1.0 m from the upstream boundary of the flume). Because of the limited size of the flume, slope a was set with a steep angle (26.8%) in all experiments. Considering the effect of instabilities from the outlet pipe and the overly steep slope, the region with slope a was excluded from numerical simulations and inverse analysis. As a result, for the production of artificial datasets, the upstream boundary of simulation was set at the end of slope a. The numerical simulation was conducted for 4.0 m downstream, but only the deposits from the upstream boundary of simulation to 2.6 m downstream were used for training and verification. This range corresponds to 1.0 m to 3.6 m from the upstream boundary of the flume, where samples were collected for experiment deposits. The range of simulation was set longer than the range used for training and verification to minimize the influence of the boundary conditions at the downstream end of simulation.

Table 3. Conditions and settings of experiments conducted with a mixture of siliciclastic sand and plastic particle.

	BS1	BS2
C_{TT}	0.0587	0.0140
C_{1T}	0.0246	0.000122
$C_{\mathrm{2T,BS}}$	0.0101	0.00385
$C_{\mathrm{2T,PP}}$	0.00958	0.00251
$C_{\mathrm{3T,BS}}$	0.00811	0.00503
$C_{\mathrm{3T,PP}}$	0.00424	0.00164
C_{4T}	0.00202	0.000846
x_{C} (m)	2.33	1.85
x_{U} (m)	2.71	2.23
x_{H} (m)	1.40	1.40
Temperature (°C)	9.5	12.2

With regard to the values of hyperparameters used during the training process, the dropout rate, validation split and momentum for DNN were set to 0.5, 0.2, and 0.9, respectively. Learning rate was set to 0.01, batch size to 32, number of layers to 5, number of nodes each layer to 2000, and epoch to 15000. With this setting the eventual validation loss was 0.0031 when training with plastic particle only datasets and 0.0020 when training with siliciclastic sand plastic particle mixture datasets. Figures 4A and 5A show that overlearning did not occur, as no deviation was observed between the resulting values of loss function for the training and validation datasets.

5.1 Verification of Inverse Model with Test Artificial Datasets

This section presents the results of verification with artificial test datasets. Results of parameter reconstructions by DNN are shown in Figures 4 and 5. Parameters reconstructed include flow duration T_{d} and flow conditions at the upstream end (flow velocity U_0, flow depth H_0, sediment concentrations $C_{i,0}$). Verification was performed separately for artificial datasets of experiments using plastic particle only and artificial datasets of experiments using a mixture of siliciclastic sand and plastic particle. The results are described in Sections 5.1.1 and 5.1.2.

5.1.1 Verification with Test Artificial Datasets for Experiments Using Plastic Particle Only

As an overall trend, the reconstructed values mostly coincided with the original values, with a few values scattering further away from the line of perfect match (the diagonal solid line) (Figure 4B, C, D, E, F, G, H). A greater degree of scattering, however, was observed for U_0 in comparison to other parameters (Figure 4D). Flow duration T_{d} exhibited a tendency of underestimation (Figure 4B). The ranges of misfit ($2s$) were relatively small for all parameters, which had $2s/C_v^*$ values under 13% (Table 4). Zero lay within the 95% confidence interval (CI) of B for all parameters, except for T_{d} and $C_{1,0}$, where the CI range lay below zero for T_{d} and above zero for $C_{1,0}$.

Table 4. Sample standard deviation and bias of the inversion result of artificial datasets for experiments using plastic particle only.

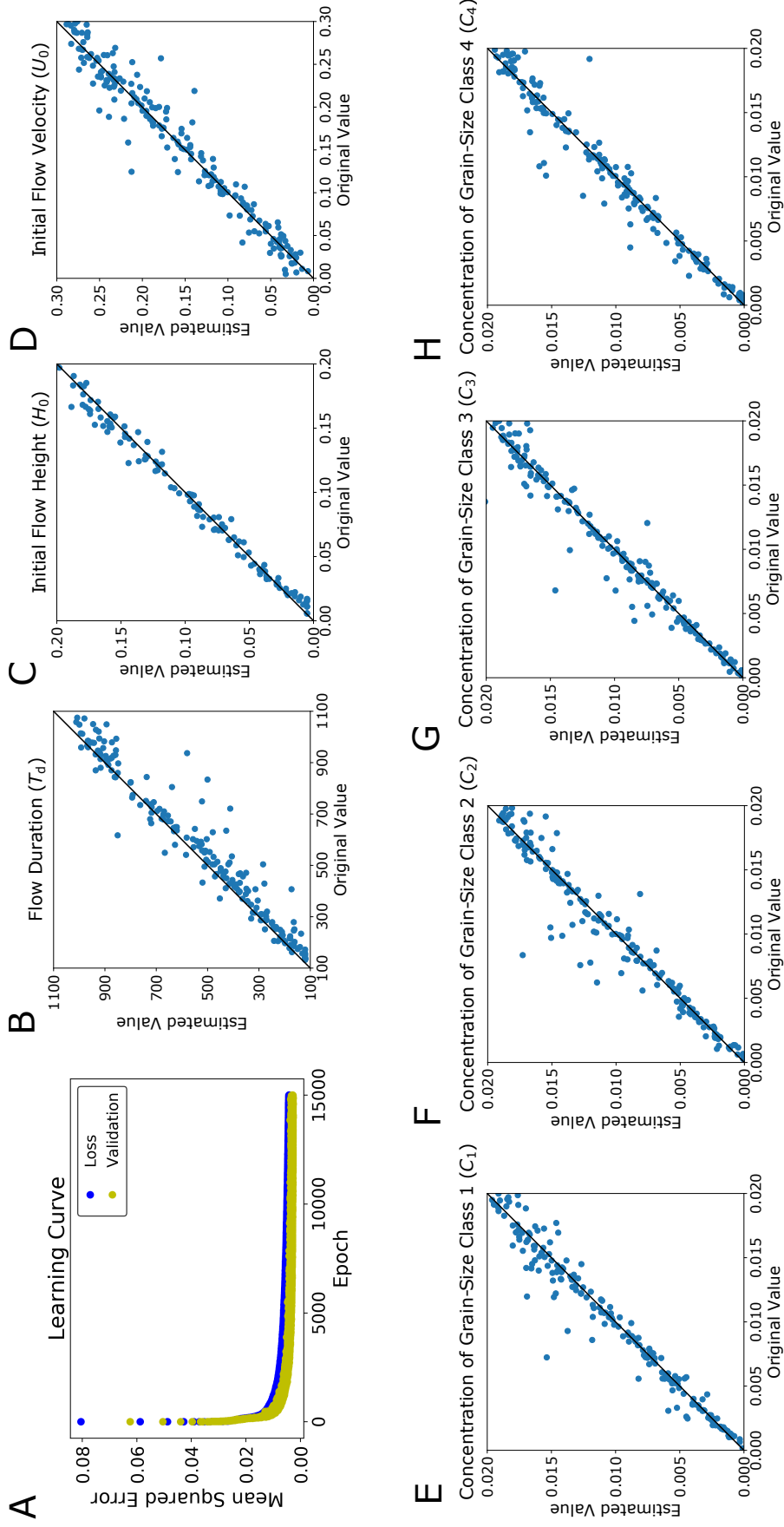| Parameters	s	C_v^*	$2s/C_v^*$	B	CI of B
U_0 (m/s)	0.0182	0.1505	0.121	-0.000673	(-0.00320, 0.00187)
H_0 (m)	0.0151	0.1525	0.0990	0.000232	(-0.00188, 0.00233)
T_d (s)	64.8	600	0.108	-36.5	(-45.6, -27.8)
$C_{1,0}$	0.00114	0.01005	0.113	0.000233	(0.0000828, 0.000396)
$C_{2,0}$	0.00135	0.01005	0.134	0.000136	(-0.0000447, 0.000332)
$C_{3,0}$	0.00115	0.01005	0.114	0.000148	(-0.00000139, 0.000314)
$C_{4,0}$	0.00117	0.01005	0.116	0.000115	(-0.0000419, 0.000274)

Figure 4. Result of verification with independent artificial datasets for plastic particle only experiments. The black diagonal line in each graph is where values on the x-axis (the true values) equal to the values on the y-axis (the estimated values). If a point lies on this line, the reconstructed value matches the true value perfectly. A. Learning curve. B. Estimates of T_d. C. Estimates of H_0. D. Estimates of U_0. E. Estimates of $C_{1,0}$. F. Estimates of $C_{2,0}$. G. Estimates of $C_{3,0}$. H. Estimates of $C_{4,0}$.

5.1.2 Verification with Test Artificial Datasets for Experiments Using Siliciclastic Sand and Plastic Particle

As an overall trend, good correlations were observed for the reconstructed values and the original values of flow parameters. The reconstructed values mostly exhibited perfect matches with the original values, with a few values scattering from the line of perfect match (the diagonal black line) (Figure 5B-J). Similar to the test datasets described in Section 5.1.1, U_0 exhibited a greater degree of scattering in comparison to the other parameters. A tendency of overestimation was also observed for U_0 (Figure 5D). T_d showed a tendency of underestimation (Figure 5B). The range of misfit ($2s$) was good for T_d, H_0, $C_{1,0}$, $C_{2,BS,0}$, $C_{2,PP,0}$, $C_{3,BS,0}$, $C_{3,PP,0}$ and $C_{4,0}$, which had $2s/C_v^*$ values under 8%. U_0 was more scattered, having $2s/C_v^*$ value of 14.2% (Table 5). Zero was included in the 95% confidence interval of B except for U_0, H_0, T_d, $C_{1,0}$, $C_{2,BS,0}$ and $C_{4,0}$, where the CI ranges lay below zero for T_d and U_0, and above zero for H_0, $C_{1,0}$, $C_{2,BS,0}$ and $C_{4,0}$.

Table 5. Sample standard deviation and bias of the inversion result of artificial datasets for experiments using a mixture of siliciclastic sand and plastic particle.

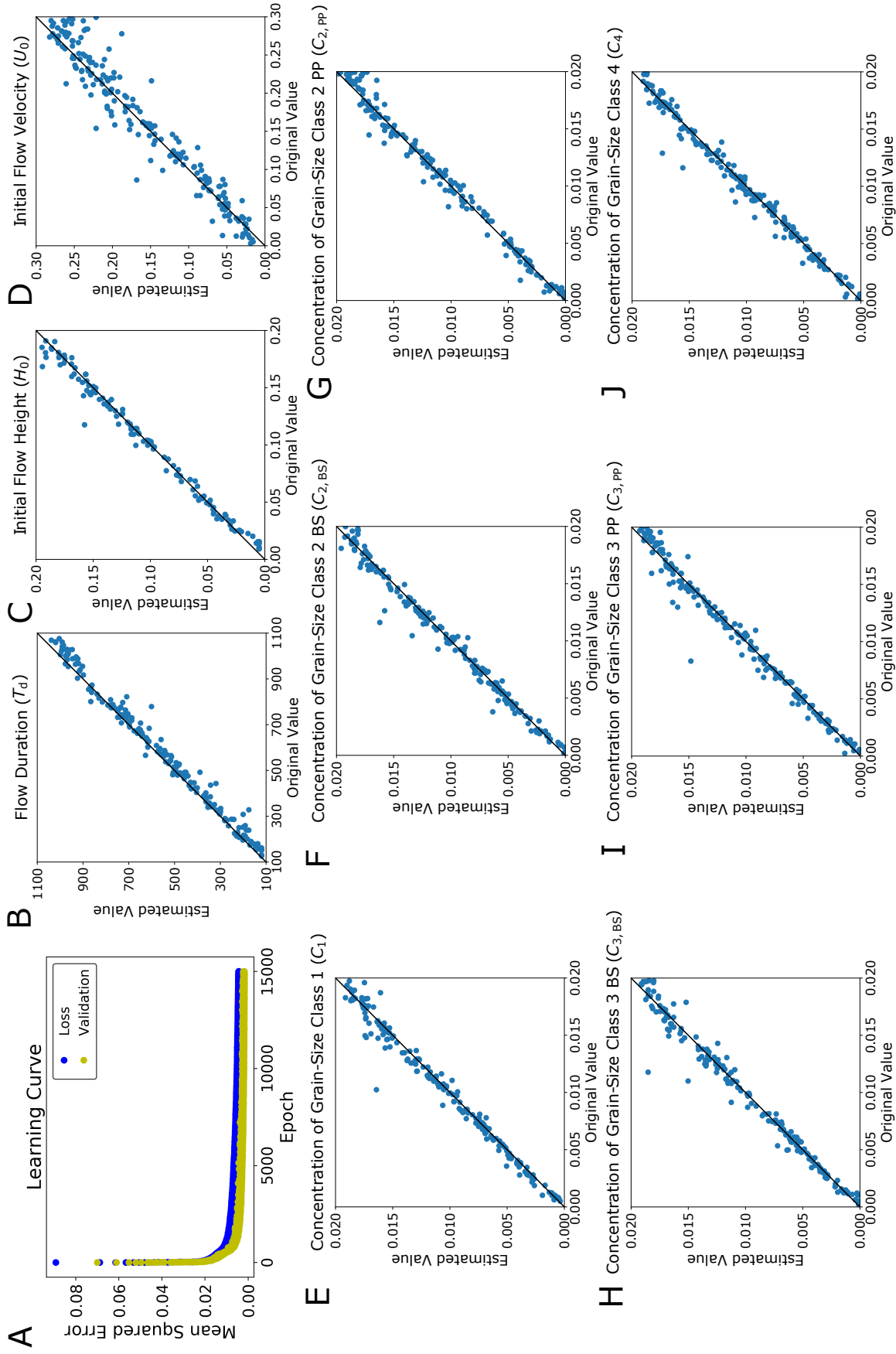| Parameters	s	C_v^*	$2s/C_v^*$	B	CI of B
U_0 (m/s)	0.0214	0.1505	0.142	-0.00413	(-0.00711, -0.00115)
H_0 (m)	0.0114	0.1525	0.0748	0.00155	(0.00000628, 0.00314)
T_d (s)	30.9	600	0.0515	-23.7	(-28.1, -19.6)
$C_{1,0}$	0.000726	0.01005	0.0722	0.000215	(0.000120, 0.000320)
$C_{2,BS,0}$	0.000692	0.01005	0.0689	0.000127	(0.0000347, 0.000230)
$C_{2,PP,0}$	0.000715	0.01005	0.0711	-0.0000752	(-0.000176, 0.0000243)
$C_{3,BS,0}$	0.000818	0.01005	0.0814	0.000105	(-0.00000385, 0.000221)
$C_{3,PP,0}$	0.000816	0.01005	0.0812	0.0000754	(-0.0000336, 0.000193)
$C_{4,0}$	0.000707	0.01005	0.0703	0.000125	(0.0000303, 0.000228)

Figure 5. Result of verification with independent artificial datasets for siliciclastic sand plastic particle mixture experiments. The black diagonal line in each graph is where values on the x-axis (the true values) equal to the values on the y-axis (the estimated values). If a point lies on this line, the reconstructed value matches the true value perfectly. A. Learning curve. B. Estimates of T_d. C. Estimates of H_0. D. Estimates of U_0. E. Estimates of $C_{1,0}$. F. Estimates of $C_{2,BS,0}$. G. Estimates of $C_{2,PP,0}$. H. Estimates of $C_{3,BS,0}$. I. Estimates of $C_{3,PP,0}$. J. Estimates of $C_{4,0}$.

5.2 Inverse Analysis of Flume Experiment Data

In this section, the deposit profiles and grain size distributions calculated are compared with the actual deposit profiles sampled from experiments (Figures 6, 8). The results of flow conditions reconstructed, including flow velocity U_{x_U}, flow height H_{x_H}, sediment concentrations C_{x_C} and flow duration $T_{\rm d}$, are compared with the values measured during the experiments (Tables 6 and 7). H_{x_H} is the flow height H at position x_H (see the positions in Table 2) downstream when the flow reached a quasi-equilibrium state. U_{x_U} is the velocity U at position x_C downstream when the flow reached a quasi-equilibrium state. C_{x_C} is the C at position x_C downstream when the flow reached a quasi-equilibrium state. Inversion results of the plastic particle only experiments (PP1, PP2) and of the experiments using a mixture of siliciclastic sand and plastic particle (BS1, BS2) are described in Sections 5.2.1 and 5.2.2.

5.2.1 Experiments using Plastic Particle Only (PP1, PP2)

Depositional profiles in these experiments exhibited a thinning and fining downstream trend with concave-upward geometry. For both runs, the reconstructed deposit profiles of the total deposition closely matched with the sampled data (Figures 6A(1), B(1)). Grain size distributions at 1.4 m and 1.8 m downstream also demonstrated good agreement for the reconstructed and measured values for both experiments (Figures 6A(2),(3), B(2),(3)), with PP2 having a slightly better match than that of PP1.

For flow height H_{x_H}, the measured and reconstructed values were in good agreement (Figure 7A). The reconstructed H_{x_H} were 0.132 m and 0.159 m for PP1 and PP2, respectively (Table 6). These values matched well with the measured values for both PP1 (0.116 m) and PP2 (0.123 m). The reconstructed U_{x_U} were 0.118 m/s (PP1) and 0.115 m/s (PP2), of which that of PP2 was close to its measured value (0.0923 m/s), whereas that of PP1 had a larger difference from its measured value (0.0608 m/s). The reconstructed values of flow duration $T_{\rm d}$ were 635 s (PP1) and 872 s (PP2), which were lower than the measured values for both PP1 (936 s) and PP2 (966 s) (Figure 7C). The reconstructed values of total concentration $C_{{\rm T},x_C}$ were 0.00587 (PP1) and 0.00383 (PP2), of which that of PP1 did not match well with the measured value of $C_{{\rm T},x_C}$ (0.000808), whereas that of PP2 was close to its corresponding measured value (0.00410). The reconstructed values of each grain-size class were good overall, but large deviations were observed for several reconstructions of concentrations that had very low measured values ($< 0.1\%$) (Figure 7D)

Table 6. Flow conditions measured and reconstructed for experiments PP1 and PP2. (R.: reconstructed, M.: Measured)

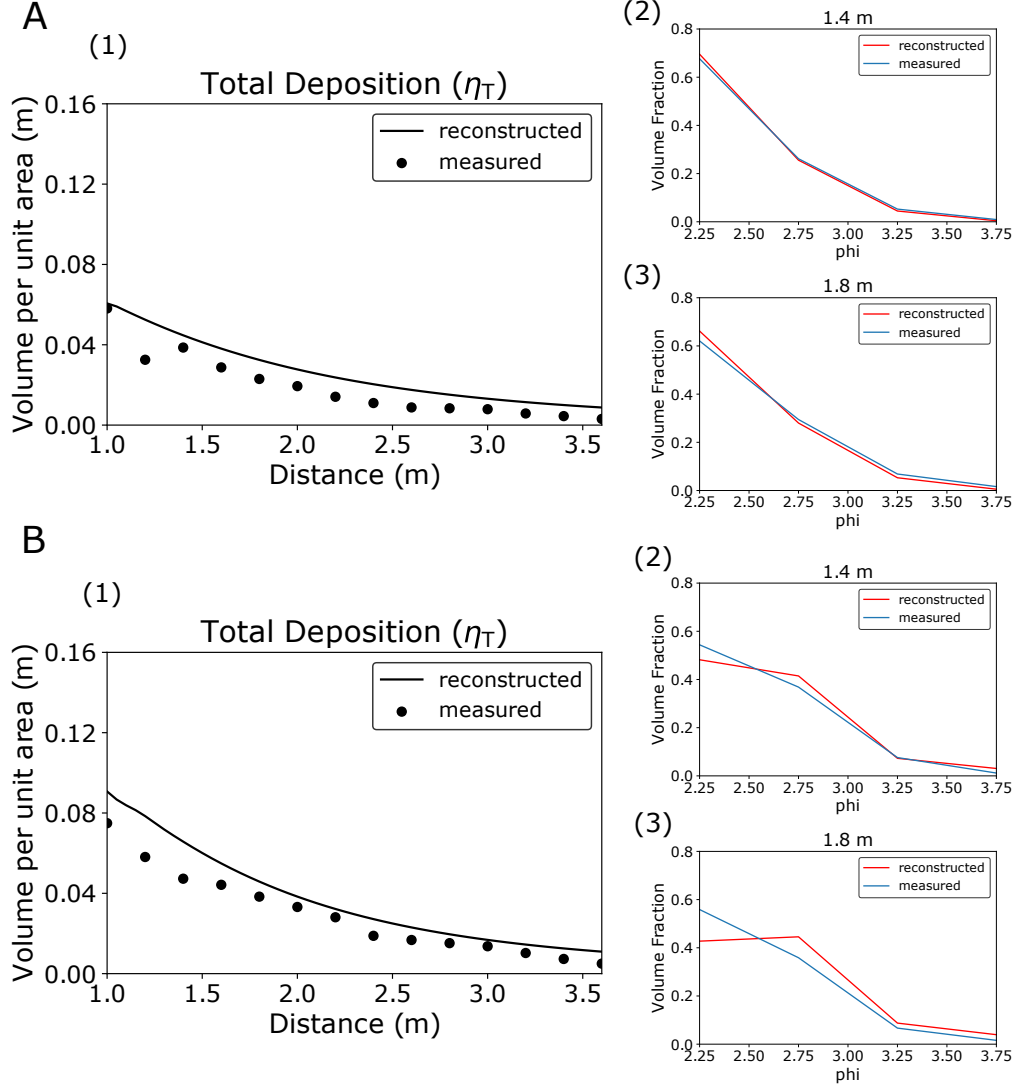| Parameters	PP1 R.	PP1 M.	PP2 R.	PP2 M.
$C_{{\rm T},x_C}$	0.00587	0.000808	0.00383	0.00410
C_{1,x_C}	0.00329	0.0000911	0.000822	0.000612
C_{2,x_C}	0.00190	0.000389	0.00173	0.00224
C_{3,x_C}	0.000576	0.000228	0.000681	0.000944
C_{4,x_C}	0.000100	0.0000999	0.000607	0.000303
H_{x_H} (m)	0.132	0.116	0.159	0.123
U_{x_U} (m/s)	0.118	0.0608	0.115	0.0923
$T_{\rm d}$ (s)	635	936	872	966

Figure 6. Reconstructed deposit profiles and the sampled deposit data of experiments PP1 and PP2. A. (1) Reconstructed and sampled η_T of PP1. (2) Grain size distribution at 1.4 m downstream. (3) Grain size distribution at 1.8 m downstream. B. (1) Reconstructed and sampled η_T of PP2. (2) Grain size distribution at 1.4 m downstream. (3) Grain size distribution at 1.8 m downstream.
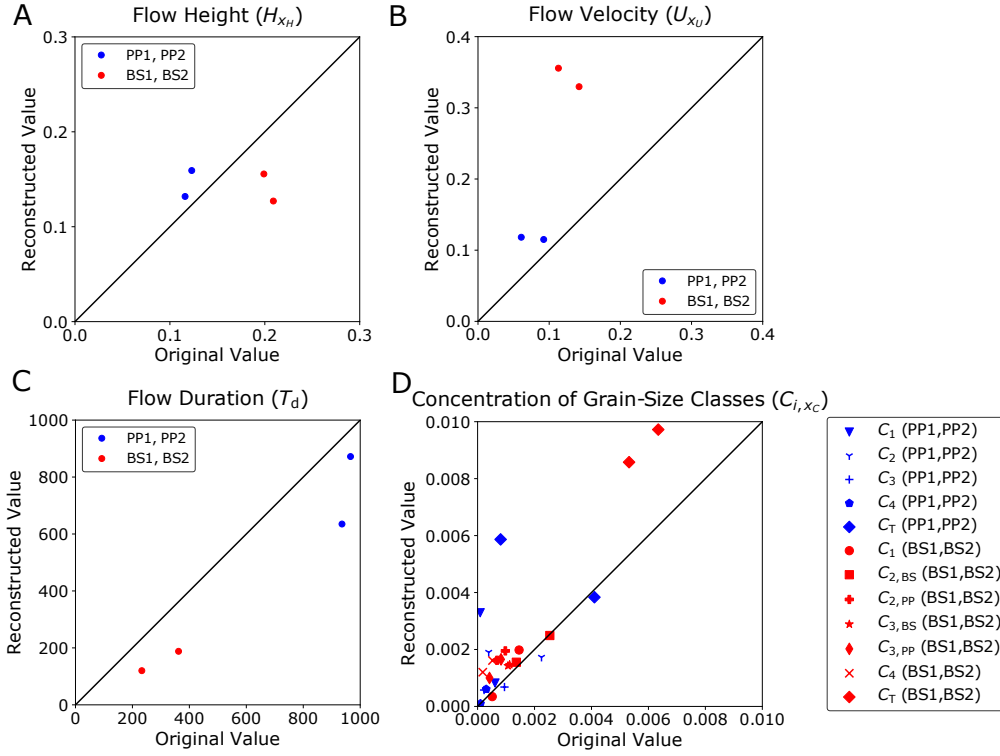
Figure 7. Reconstructed vs measured flow conditions for experiments PP1, PP2, BS1 and BS2. A. Plot for H_{x_H}. B. Plot for U_{x_U}. C. Plot for T_d. D. Plot for C_{i,x_C}.

5.2.2 *Experiments Using a Mixture of Siliciclastic Sand and Plastic Particle (BS1, BS2)*

Similar to the results for the experiments using plastic particle only, all depositional profiles in these experiments exhibited a thinning and fining downstream trend. For both experiments, the reconstructed deposit profiles of the total deposition matched closely with the sampled data (Figures 8A(1), B(1)). Grain size distributions at 1.3 m and 1.7 m downstream also demonstrated good agreement for the reconstructed and measured values for both experiments (Figures 6A(2),(3), B(2),(3)).

The reconstructed values of flow height H_{x_H} were 0.127 m and 0.156 m for BS1 and BS2, respectively (Table 7). Of these values, that for BS2 was relatively close to the measured value (0.199 m), whereas that for BS1 differs from its measured value (0.209 m). The reconstructed flow velocities U_{x_U} were 0.330 m/s (BS1) and 0.356 m/s (BS2), which did not match well with the measured values 0.142 m/s (BS1) and 0.113 m/s (BS2) (Figure 7B). The reconstructed flow durations T_d were 188 s (BS1) and 120 s (BS2), which were relatively close to the measured values for both BS1 (362 s) and BS2 (233 s). The reconstructed values of total concentration C_{T,x_C} were 0.00858 (BS1) and 0.00972 (BS2), which also matched relatively well for both experiments BS1 (0.00532) and BS2 (0.00635). The reconstructed values of each grain-size class were mostly reasonable, but large deviations were observed for several reconstructions of concentrations with very low measured values ($< 0.1\%$) (Figure 7D).
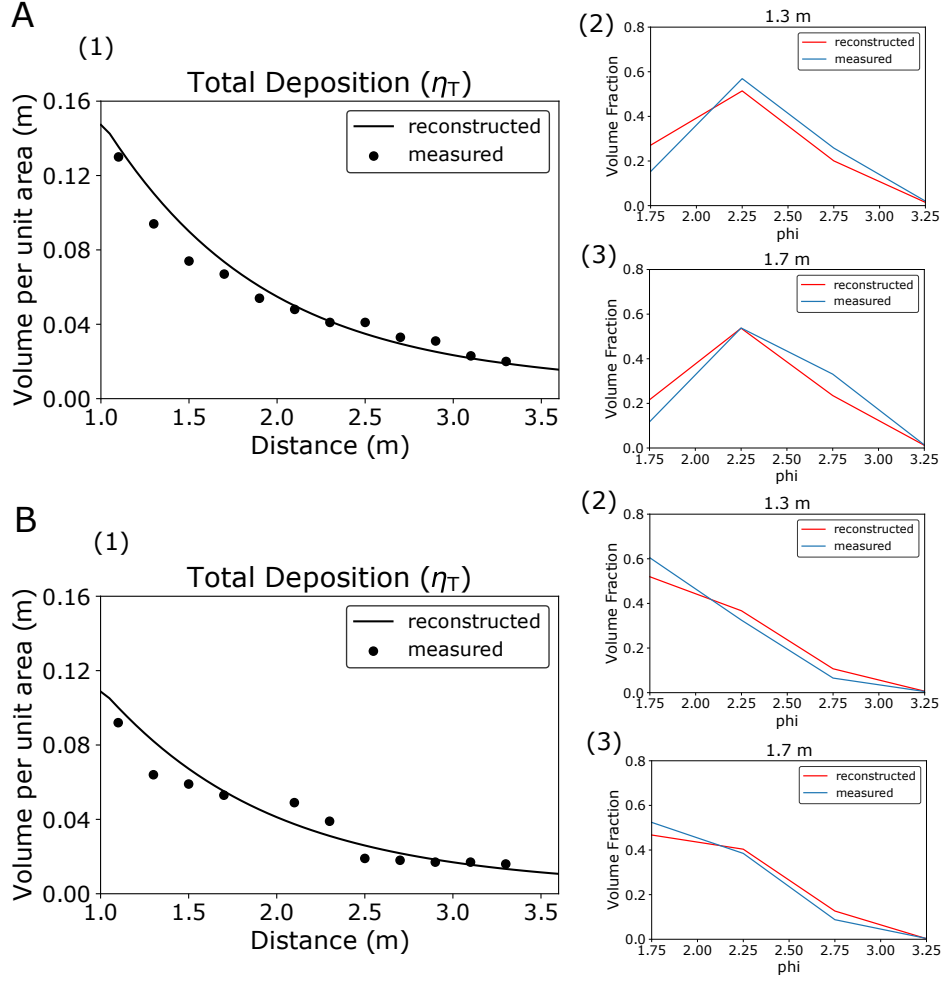
Figure 8. Reconstructed deposit profiles and the sampled deposit data of experiments BS1 and BS2. A. (1) Reconstructed and sampled η_T of BS1. (2) Grain size distribution at 1.4 m downstream. (3) Grain size distribution at 1.8 m downstream. B. (1) Reconstructed and sampled η_T of BS2. (2) Grain size distribution at 1.4 m downstream. (3) Grain size distribution at 1.8 m downstream.

Table 7. Flow conditions measured and reconstructed for experiments BS1 and BS2. (R.: reconstructed, M.: Measured)

Parameters	BS1 R.	BS1 M.	BS2 R.	BS2 M.
C_{T,x_C}	0.00858	0.00532	0.00972	0.00635
C_{1,x_C}	0.000345	0.000514	0.00198	0.00146
C_{2,BS,x_C}	0.00155	0.00136	0.00249	0.00254
C_{2,PP,x_C}	0.00195	0.000974	0.00162	0.000686
C_{3,BS,x_C}	0.00147	0.00113	0.00143	0.00107
C_{3,PP,x_C}	0.00165	0.000823	0.00100	0.000418
C_{4,x_C}	0.00161	0.000523	0.00120	0.000182
H_{x_H} (m)	0.127	0.209	0.156	0.199
U_{x_U} (m/s)	0.330	0.142	0.356	0.113
T_{d} (s)	188	362	120	233

6 Discussion

6.1 Validation of DNN as an Inversion Method for Turbidity Currents by Artificial Test Datasets

The results from verification with artificial datasets proved the ability of DNN to reasonably reconstruct the hydraulic conditions of turbidity current from its turbidite deposits. Reconstructions of initial flow conditions and the flow duration for artificial datasets (Sections 5.1.1 and 5.1.2) were good overall judging from the s and B values (Tables 4 and 5). The reconstructions of the flow duration T_{d}, flow depth H_0, velocity U_0, and sediment concentrations $C_{1,0}$, $C_{2,0}$ ($C_{2,\mathrm{BS},0}$ and $C_{2,\mathrm{PP},0}$ for mixture experiments), $C_{3,0}$ ($C_{3,\mathrm{BS},0}$ and $C_{3,\mathrm{PP},0}$ for mixture experiments), and $C_{4,0}$ were high in precision (Tables 4 and 5).

Overall, the correlations between the true and reconstructed values were obvious for all parameters reconstructed. Some scattering was observed for the reconstructed parameters, but most values stayed close within the range of perfect reconstruction. The range of misfit $2s$ of all parameters lies below 14.3% of the matching representative value (Tables 4 and 5). A relatively greater degree of scattering is observed for U in comparison to the other parameters (Figures 4D and 5D).

With regard to the estimation bias, zero was included in the 95% confidence interval of bias for most of the parameters, proving that the reconstructed values were not significantly biased with respect to the original values. Even among the parameters where statistically significant biases were detected, their deviations were minor in comparison to the representative values of the parameters (Table 4 and 5). For example, in both artificial datasets using plastic particle only and mixture of siliciclastic sand and plastic particles, the estimation bias B for T_{d} had a negative value and the range of the confidence interval of B was below zero (Tables 4 and 5), indicating a tendency of underestimation for T_{d}. However, the bias for T_{d} was only 3.95% (mixture experiments) or 6.08% (plastic particle only) of the representative value of this parameter (600 s).

Thus, it can be said that this method is suitable for estimating the paleo-hydraulic conditions of actual turbidity currents. Reconstructed parameters are well correlated without any serious biases from true original values, implying that the in-

verse model produced in this study serves as a high precision, high accuracy estimator of flow conditions.

6.2 Verification of DNN Inversion with Flume Experiment Data

As a result of inversion using DNN, the overall deposit profiles were well reconstructed for all four experiments, and the reconstructed grain size distribution downstream matched with the grain size distribution sampled from experimental deposits (Figures 6 and 8). DNN as an inverse method tries to find the combination of hydraulic conditions that best produces the deposit profiles inputted. The fact that the reconstructed hydraulic conditions accurately reproduced the deposit profiles used for inverse analysis indicates good performance by DNN with the inverse model.

Furthermore, the hydraulic conditions and flow duration reconstructed mostly lie within a reasonable range from the line of perfect reconstruction (Figure 7). Among the reconstructed hydraulic conditions, flow heights H_{x_H} were well reconstructed for all four experiments (Table 6 and 7). The differences between the reconstructed and measured values of H_{x_H} were less than 39.2%. The layer-averaged models with top-hat assumption (all shape factors are assumed to be unity) inevitably exhibit inaccuracies in the flow parameters due to their simplification of flow dynamics. Indeed, in previous experimental studies of the shallow water model, up to 50% deviation from the measured values was observed for the calculated flow heights (Parker et al., 1987; Kostic & Parker, 2006). Considering the limitation of this model, the reconstructed flow heights in this study can be interpreted as reasonable estimates of the experimental results.

Flow durations T_d were also reasonably reconstructed but were underestimated for all four experiments, as observed for the artificial test datasets. The reconstructed concentration of each grain-size class C_{i,x_C} was scattered especially when the measured values were very low ($< 0.1\%$), but the total concentrations of sediment exhibit relatively good agreement with the experimental values. In contrast to other parameters, flow velocities U_{x_U} were largely overestimated for all four experiments. Difference between the reconstructed and measured U_{x_U} range from 24.6% to 215% of the measured values. Up to 25% deviation from the measured value was observed in previous research (Kostic & Parker, 2006), but deviation in this case exceeds that of the previous research.

One potential reason behind the deviations in the reconstructed values is that inverse analysis itself is essentially difficult for turbidity currents. For instance, flow parameters cannot be reconstructed when different combinations of initial conditions produce exactly the same deposit profile. However, this is unlikely because flows with a wide variety of initial conditions were tested with artificial datasets and the reconstructions were mostly reasonable, proving the ability of DNN to distinguish minor differences in the characteristics of deposits. Instead, sources of deviation could lie in the forward model employed in this study.

Through analysis of the result of application of DNN to flume experiment data, it became clear that there are three aspects for deviations in the reconstruction of hydraulic conditions: (1) bias inherent in the inverse model, (2) measurement errors during the experiments, and (3) inaccuracy within the forward model of turbidity currents employed in this study.

(1) Regarding the inherent bias in the inverse model, T_d reconstructed for the flume experiments exhibited the same tendencies of deviation during the reconstruction of artificial test datasets. Thus, deviation in the reconstruction of T_d may be considered as a systematic error originating from the internal settings of DNN. U_{x_U} exhibited similar tendencies in artificial datasets reconstruction to those in flume experiment reconstruction, but the deviation of U_{x_U} was so large for U_{x_U} in flume experiment

reconstruction that it seems unlikely to have originated solely from the DNN model. The tendencies of deviation for C_i in the reconstruction of flume experiment datasets did not match those for the artificial datasets, and thus also did not occur because of the tendencies of the inverse model.

(2) The main source of deviation for sediment concentrations C_i may be inaccuracies in the measurements. As shown in Figure 7, some of the measured concentrations C_i were extremely small ($< 0.1\%$), making them susceptible to minor disturbances during sampling and measurements. For values that are extremely small, even minor deviations appear to be large. Thus, for C_i, the main source of deviation may not be the reconstructed values but the measured values.

(3) Inaccuracy in the forward model in describing the physical processes of turbidity currents may account for deviations of the reconstructed flow velocities from the measured values. There are several potential reasons to why the reconstruction of flow velocity did not go as well as with the other parameters, but the most probable reason is the inaccuracy of the entrainment function in describing the actual effect of entrainment in flow, considering that the exponent in the calculation of dimensionless vertical velocity in the entrainment function was determined purely by optimization and differed greatly in previous studies (Parker et al., 1987; Garcia & Parker, 1991; Dorrell et al., 2018). Another problem may lie in the layer averaging of flow velocity. Even though the model uses layer averaged flow velocity for calculation, a recent study by (Luchi et al., 2018) had pointed out that a two layer model is more suitable for the calculation of turbidity currents. This research aims to verify DNN as a method of inverse analysis of turbidity currents. Improvement of the forward model, including entrainment function and velocity calculation, should be the next step in the inverse analysis study of turbidity currents.

The shallow water model implemented holds certain limitations due to its simplified calculation of flow dynamics. Nevertheless, the simplifications make it possible to perform large batches of natural scale simulations. Overall, even though a certain amount of deviation was observed for all parameters, they lie mostly within a reasonable range for the eventual purpose of application to natural scale turbidity currents.

6.3 Comparison of DNN with Existing Methodologies

In comparison to previous methods of inverse analysis of turbidity currents, the inversion method using DNN holds great advantage in terms of calculation cost and in terms of accuracy of reconstruction. Previous inversion methods of turbidity currents seek to optimize the initial conditions to a particular set of data collected from turbidite, which is extremely time-consuming to apply to one dataset and does not guarantee the general applicability of the method to turbidite deposits (Lesshafft & Marquet, 2010; Parkinson et al., 2017; Nakao & Naruse, 2017). For example, genetic algorithm applied in Nakao and Naruse (2017) first initializes a population of parameters and then optimizes the population of parameters through selection and mutation. Eventually, the parameters left can successfully reconstruct the target turbidite. However, each epoch of optimization requires the results of selection from the previous epoch, and thus the calculation of the forward model cannot be parallelized over epochs. In adjoint method used by Parkinson et al. (2017), control variables within the forward model of turbidity currents are first initialized and inputted into the numerical model. The turbidite deposit profile is calculated and compared with the target values using a cost function. Gradients of the cost function (objective function) for control variables are calculated analytically. If the result is decided to be less than optimal, the adjoint model will run and control variables will be adjusted by descent method. The adjusted control variables will again be inputted into the numerical model. This cycle is repeated until the reconstructed deposit profile is judged

to be optimal, thus the iteration of calculation cannot be performed simultaneously. By contrast, DNN explores the general functional relationship between the turbidite deposited and the current, making it applicable to turbidity currents in general. Forward model calculation to produce training datasets can be perfectly parallelized, such that the amount of time needed for calculation reduces greatly.

Since parallelization of forward model calculation greatly reduced the time for calculation, a more accurate and realistic forward model with heavier calculation load was able to be implemented. As a result, the forward model used in this research is much better at capturing the spatio-temporal evolution of turbidity current in comparison to forward model used in previous research (Falcini et al., 2009; Parkinson et al., 2017). Falcini et al. (2009) used a steady flow forward model, whereas our forward model is a non-steady flow model that reproduces the evolution of flow over time. The method implemented in Parkinson et al. (2017) omitted the effect of entrainment, a significant part of sediment transport in turbidity currents. As a result, their reconstructed values of flow height, concentration, and grain diameter of the turbidite were 2.56 km, 0.0494%, and 103 μm, respectively (Parkinson et al., 2017). These values were largely off the expected range when examined based on the objective values collected from the turbidite deposits. By contrast, our predictions lie relatively close to the original values collected and the effect of sediment suspension was incorporated in our forward model. Another improvement from previous research is that the forward model used in this case applies to turbidite datasets of multiple grain-size classes.

By contrast, Lesshafft and Marquet (2010) proposed a method based on direct numerical simulation (DNS) of the Navier-Stokes equations. However, the calculation costs of the method were extremely high, making it unrealistic to apply the method to natural scale turbidites. The computational cost of DNS was scaled to Re^3, thus limiting the effectiveness of DNS to only experimental scale flows (Biegert et al., 2017). As a result, the maximum value of Reynolds number attained in previous numerical simulation using DNS was 15,000 (Cantero et al., 2007), which corresponds to 3.0 cm/s for velocity and 50 cm for flow height. Thus, their methodology cannot be applied to natural scale turbidites.

7 Conclusions

In this study, a new method for the inverse analysis of turbidite using DNN was verified with actual flume experiment data. In comparison to previous methods, DNN proved to be an efficient method for inversion of turbidity currents without compromising the accuracy of reconstruction. DNN performed well for verification with artificial datasets, judging by the standard deviation and bias of the reconstructed parameters. In terms of the application of DNN to experiment data, deposit profiles were well reconstructed; however, the initial flow conditions did not match the measured values perfectly.

The reconstructed flow heights H for PP1 and PP2 were 0.132 m and 0.159 m, respectively, which were good matches with the measured values 0.116 m and 0.123 m. H reconstructed for BS1 and BS2 were 0.127 m and 0.156 m, respectively, and H measured were 0.209 m and 0.199 m, which exhibited larger differences than those for PP1 and PP2 but were still reasonable. H was underestimated for BS1 and BS2. On the other hand, T_d was underestimated for all experiments. For BS1 and BS2 the reconstructed values were 188 s and 120s, respectively, and measured values were 362 s and 233 s. For PP1 and PP2, the reconstructed values were 635 s and 872 s, respectively, and the measured values were 936 s and 966 s. U was overestimated for all experiments, with PP1 and PP2 better reconstructed than BS1 and BS2. The reconstructed U for PP1 and PP2 were 0.118 m/s and 0.115 m/s, respectively, and measured values were 0.0608 m/s and 0.0923 m/s. The reconstructed U for BS1 and

BS2 were 0.330 m/s and 0.356 m/s, respectively, and measured values were 0.142 m/s and 0.113 m/s.

Overall, DNN exhibited good performance for the inversion of artificial datasets and some parameters of the experiment data. The deposit profiles were well reconstructed, indicating the success of DNN in the exploration of the functional relationship between the initial conditions of flow and the resulting deposits. The results of verification with artificial datasets and flume experiments reveal that the implemented forward model is competent in performing inverse analysis on turbidity currents, but needs to be more robust for application to a wide range of flow conditions. Improvement of forward models and parameters such as the entrainment function will be top priority in the future. Hyperparameter settings and internal structure of DNN also have room for improvement judging from the inversion result of artificial datasets. Application of DNN to field datasets will be the eventual goal.

Appendix A Details of Forward Model Implemented

A1 Example of Forward Model Calculation

The forward model was tested with two sets of numerical simulations of turbidity currents. Testing was conducted using the forward model programmed for the production of artificial datasets for plastic particle only experiments. The settings of the numerical simulations are listed in Table A1, whereas the time evolution of the high $C_{T,0}$, U_0 simulation is shown in Figure A1 and the time evolution of the low $C_{T,0}$, U_0 simulation is shown in Figure A2. In both cases, flow height H was greater toward the head of the current. H at the head of the current also grew over time (Figures A1A and A2A). Flow velocity U in the high $C_{T,0}$, U_0 simulation increased when the current propagated downstream (Figure A1B), while U in the low $C_{T,0}$, U_0 simulation increased initially then decreased as the current propagated (Figure A2B). The total volumetric concentration of sediment C_T in flow decreased downstream in both cases (Figures A1C and A2C). In the high $C_{T,0}$, U_0 case, a larger portion of sediment was deposited downstream than in the low $C_{T,0}$, U_0 case (Figures A1D and A2D). The low $C_{T,0}$, U_0 case had the most sediment deposited toward the upstream end of flow.

For the high $C_{T,0}$, U_0 simulation, a thicker deposit was observed for grain-size class 1 than for grain-size classes 3 and 4 (Figures A1E,G,H). Even though the initial concentrations of the finer grain-size classes 3 and 4 $C_{3,0}$, $C_{4,0}$ were higher than that of the coarser grain-size class 1 ($C_{1,0}$), less fine sediment was deposited since it was more likely to stay suspended and be carried beyond the lower flow boundary by the high-velocity flow. For the low $C_{T,0}$, U_0 simulation, the grain-size class with a thicker deposit has a higher initial concentration. The coarsest grain-size class, grain-size class 1, had almost all sediment deposited near the upstream boundary, while the finest grain-size class, grain-size class 4, had sediment spread out toward the downstream direction (Figures A2E,H). This happened because the low-velocity flow was unable to keep the coarse sediment suspended.

Table A1.   Initial flow conditions of numerical simulations of turbidity currents.

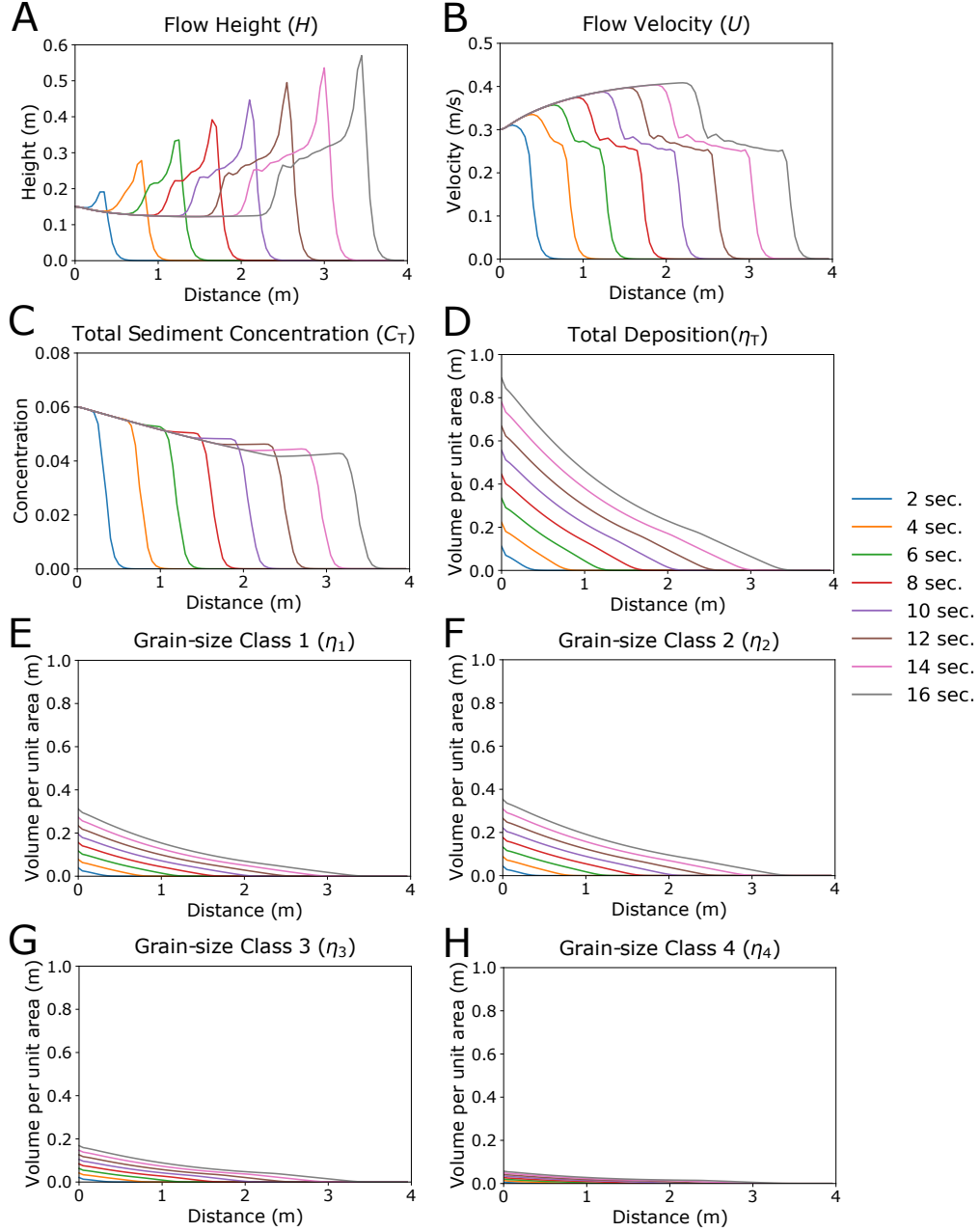|	High $C_{T,0}$, U_0	Low $C_{T,0}$, U_0
H_0 (m)	0.15	0.15
U_0 (m/s)	0.3	0.03
$C_{T,0}$	0.06	0.005
$C_{1,0}$	0.01	0.00025
$C_{2,0}$	0.02	0.0025
$C_{3,0}$	0.018	0.00175
$C_{4,0}$	0.012	0.0005
c_f	0.002	0.002
r_o	1.5	1.5
Duration (s)	420	420

Figure A1. Example of forward model calculation with high initial flow velocity and sediment concentration (Table A1). A. Time evolution of flow height H. B. Time evolution of flow velocity U. C. Time evolution of total sediment volumetric concentration C_T. D. Time evolution of deposit profile η_T. E. Time evolution deposit profile of grain-size class 1 η_1. F. Time evolution of deposit profile of grain-size class 2 η_1. G. Time evolution of deposit profile of grain-size class 3 η_1. H. Time evolution of deposit profile of grain-size class 4 η_1.
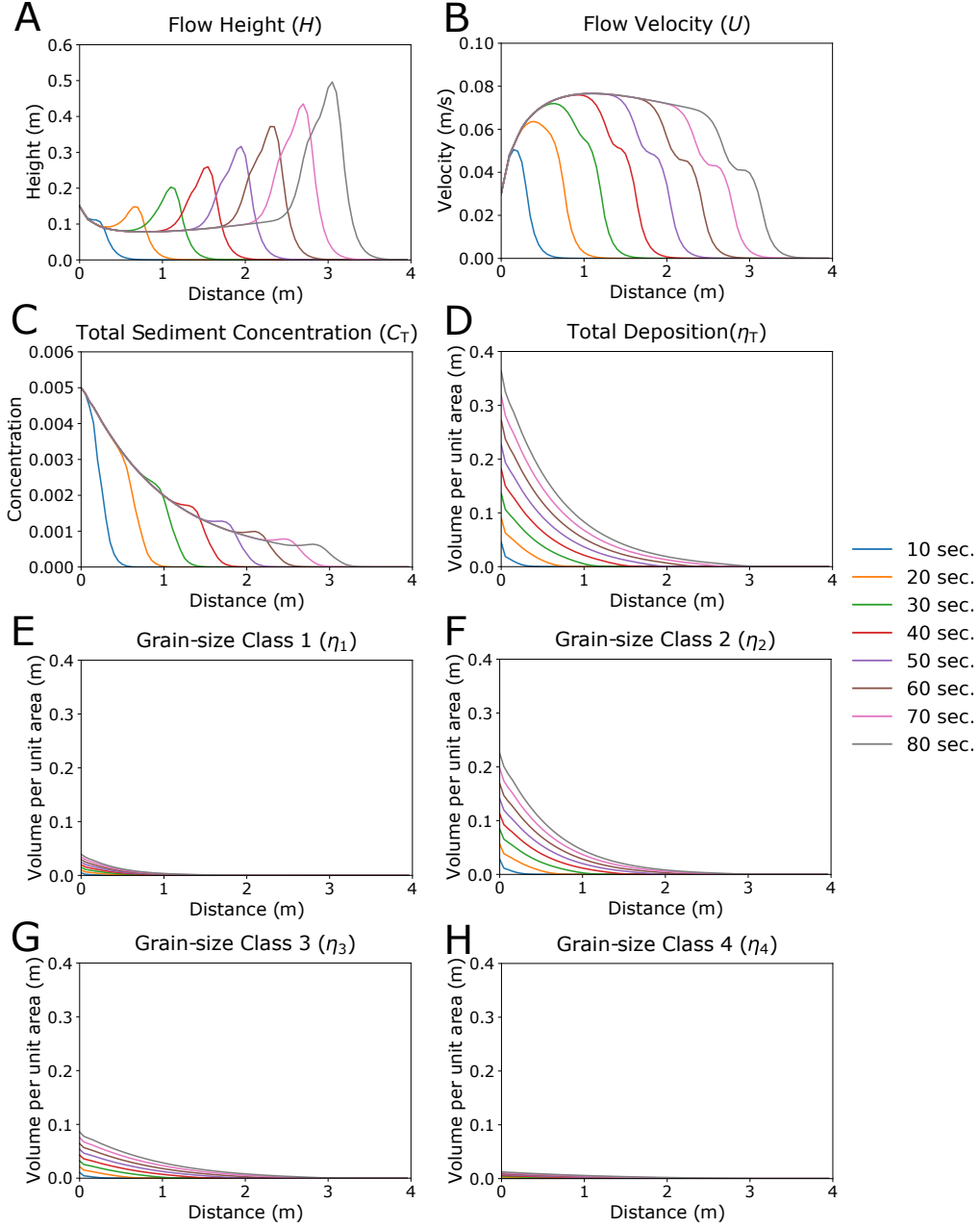
Figure A2. Example of forward model calculation with low initial flow velocity and sediment concentration (Table A1). A. Time evolution of flow height H. B. Time evolution of flow velocity U. C. Time evolution of total sediment volumetric concentration C_T. D. Time evolution of deposit profile η_T. E. Time evolution deposit profile of grain-size class 1 η_1. F. Time evolution of deposit profile of grain-size class 2 η_1. G. Time evolution of deposit profile of grain-size class 3 η_1. H. Time evolution of deposit profile of grain-size class 4 η_1.

A2 Sensitivity Tests of Forward Model

The degree of sensitivity of the forward model against changes in the initial conditions of the flow and model parameters was tested (Table A2). Testing was conducted using the forward model programmed for the production of artificial datasets of plastic particle only experiments. Numerical simulations were conducted with different values of the six parameters H_0, U_0, $C_{T,0}$, e_s, r_o, c_f. Other parameters were unchanged for the simulations.

The results of the sensitivity tests revealed that changes in deposit profile occurs when the initial flow conditions differ (Figure A3). The volume of sediment deposited increased overall as H_0 increased (Figure A3A). The same trend was observed for U_0, and $C_{T,0}$ (Figure A3B, C). Out of these three parameters, the amount of increase in deposit thickness was greatest for $C_{T,0}$, and smallest for U_0. With regard to model closure parameters, the resultant deposit profile exhibited nearly no change for different values of entrainment coefficient e_s (Figure A3D). Slightly lower amount of deposition was observed for greater e_s. An increase in the amount of deposition was observed as c_f decreased (Figure A3F). The thickness of deposit increased moderately when r_o increased.

Table A2. Settings for sensitivity tests of forward model.

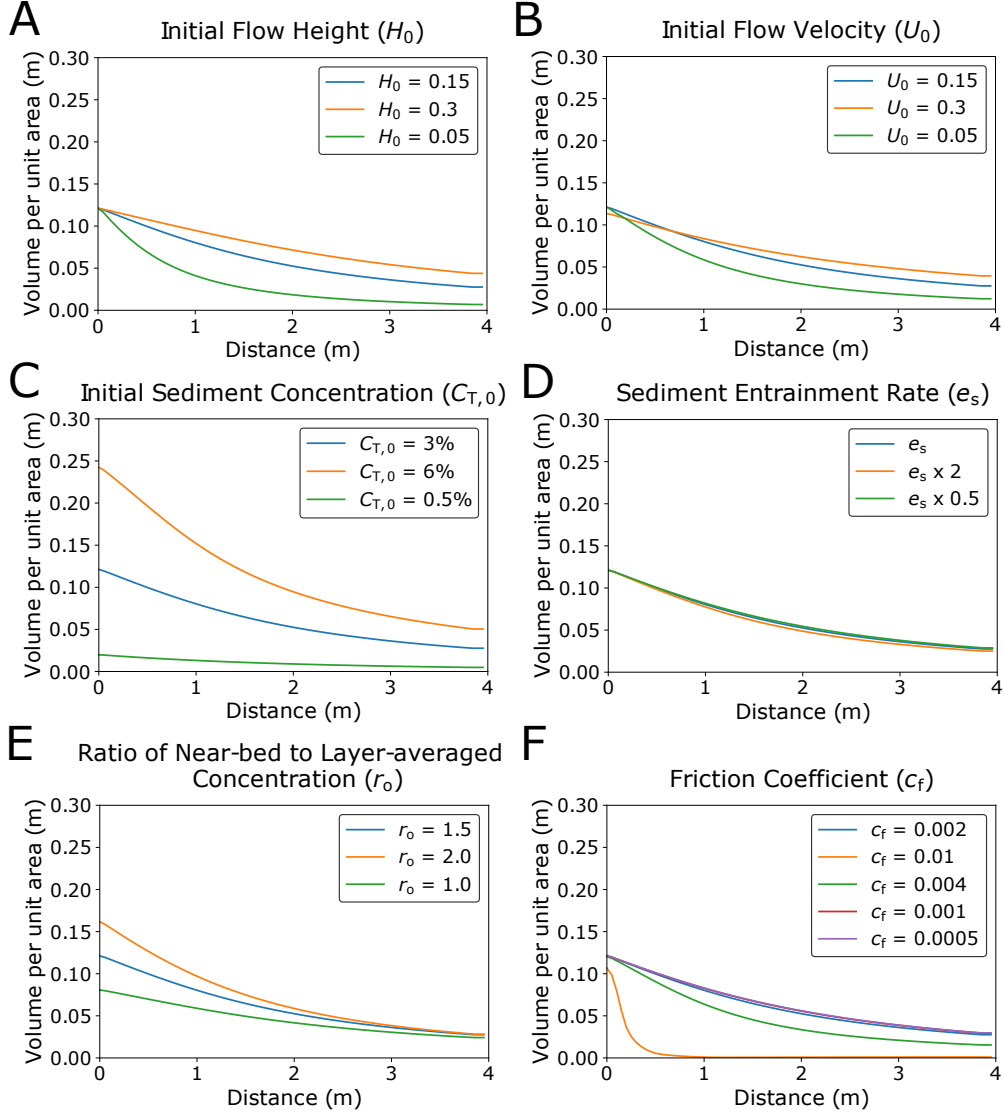| Case	H_0 (m)	U_0 (m/s)	$C_{T,0}$	e_s	r_o	c_f
1	0.15	0.15	0.03	GP	1.5	0.002
2	0.3	0.15	0.03	GP	1.5	0.002
3	0.05	0.15	0.03	GP	1.5	0.002
4	0.15	0.3	0.03	GP	1.5	0.002
5	0.15	0.05	0.03	GP	1.5	0.002
6	0.15	0.15	0.06	GP	1.5	0.002
7	0.15	0.15	0.005	GP	1.5	0.002
8	0.15	0.15	0.03	GPx2	1.5	0.002
9	0.15	0.15	0.03	GPx0.5	1.5	0.002
10	0.15	0.15	0.03	GP	2.0	0.002
11	0.15	0.15	0.03	GP	1.0	0.002
12	0.15	0.15	0.03	GP	1.5	0.01
13	0.15	0.15	0.03	GP	1.5	0.004
14	0.15	0.15	0.03	GP	1.5	0.001
15	0.15	0.15	0.03	GP	1.5	0.0005

Figure A3. Sensitivity tests of deposit profile of artificial turbidites against change in initial flow conditions and closure parameters (Table A2). A. Dependency on initial flow height H_0. B. Dependency on initial flow velocity U_0. C. Dependency on initial total sediment volumetric concentration $C_{T,0}$. D. Dependency on sediment entrainment rate e_s. E. Dependency on ratio of near-bed to layer-averaged concentration r_o. F. Dependency on friction coefficient c_f.

Notation

$\boldsymbol{\alpha_1}$, $\boldsymbol{\alpha_2}$ Parameters related to sediment entrainment

$\boldsymbol{c_f}$ Friction coefficient

$\boldsymbol{C_i}$ Layer-averaged volumetric concentration of suspended sediment of the ith grain-size class

$\boldsymbol{C_T}$ Layer-averaged total concentration of suspended sediment

$\boldsymbol{D_i}$ Representative grain diameter of the ith grain-size class

$\boldsymbol{e_{si}}$ Entrainment rate of sediment of the ith grain-size class into suspension

$\boldsymbol{e_w}$ Entrainment rate of ambient water to flow

$\boldsymbol{F_i}$ Volume fraction of the ith grain-size class in active layer

$\boldsymbol{g}$ Gravitational acceleration

$\boldsymbol{H}$ Flow height

$\boldsymbol{L_a}$ Active layer thickness

$\boldsymbol{R}$ Submerged specific density of sediment

$\boldsymbol{R_{fi}}$ Dimensionless particle fall velocity of the ith grain-size class

$\boldsymbol{Re_{pi}}$ Particle Reynolds number of the ith grain-size class

$\boldsymbol{r_o}$ Ratio of near-bed suspended sediment concentration to the layer-averaged concentration of suspended sediment

$\boldsymbol{S}$ Slope gradient

$\boldsymbol{S_f}$ Friction slope

$\boldsymbol{t}$ Time

$\boldsymbol{T_d}$ Flow duration

$\boldsymbol{U}$ Layer-averaged flow velocity

$\boldsymbol{u_*}$ Shear velocity

$\boldsymbol{w_i}$ Settling velocity of a sediment particle of the ith grain-size class

$\boldsymbol{x}$ Streamwise distance

$\boldsymbol{\eta_i}$ Volume per unit area of bed sediment of the ith grain-size class

$\boldsymbol{\eta_T}$ Total volume per unit area of bed sediment

$\boldsymbol{\kappa}$ Parameter related to artificial viscosity

$\boldsymbol{\lambda_p}$ Porosity of bed sediment

$\boldsymbol{\mu}$ Dynamic viscosity of water

$\boldsymbol{\nu}$ Kinematic viscosity of water

$\boldsymbol{\rho}$ Density of water

References

Abadi, M., Agarwal, A., Barham, P., Brevdo, E., Chen, Z., Citro, C., . . . Zheng, X. (2015). *TensorFlow: Large-scale machine learning on heterogeneous systems.* Retrieved from `http://tensorflow.org/` (Software available from tensorflow.org)

Altinakar, M., Graf, W., & Hopfinger, E. (1996). Flow structure in turbidity currents. *Journal of Hydraulic Research*, *34*(5), 713-718. Retrieved from `https://doi.org/10.1080/00221689609498467` doi: 10.1080/00221689609498467

Arai, K., Naruse, H., Miura, R., Kawamura, K., Hino, R., Ito, Y., . . . Kasaya, T. (2013, 11). Tsunami-generated turbidity current of the 2011 tohoku-oki earth-

quake. *Geology*, *41*(11), 1195–1198.

Baas, J. H., Van Dam, R. L., & Storms, J. E. A. (2000). Duration of deposition from decelerating high-density turbidity currents. *Sedimentary Geology*, *136*(1), 71–88.

Biegert, E., Vowinckel, B., Ouillon, R., & Meiburg, E. (2017). High-resolution simulations of turbidity currents. *Progress in Earth and Planetary Science*, *4*(1), 33.

Bottou, L. (2010). Large-scale machine learning with stochastic gradient descent. In Y. Lechevallier & G. Saporta (Eds.), *Proceedings of compstat'2010* (pp. 177–186). Heidelberg: Physica-Verlag HD.

Bouma, A. H. (1962). *Sedimentology of some flysch deposits: A graphic approach to facies interpretation.* Elsevier.

Cantero, M. I., Balachandar, S., & Garcia, M. H. (2007). High-resolution simulations of cylindrical density currents. *Journal of Fluid Mechanics*, *590*, 437–469.

Daly, R. A. (1936). Origin of submarine canyons. *American Journal of Science*, *31*(186), 401–420.

Davison, A. C., & Hinkley, D. V. (1997). *Bootstrap methods and their application.* Cambridge University Press. doi: 10.1017/CBO9780511802843

Dietrich, W. E. (1982). Settling velocity of natural particles. *Water Resources Research*, *18*(6), 1615–1626. doi: 10.1029/WR018i006p01615

Dorrell, R. M., Amy, L. A., Peakall, J., & McCaffrey, W. D. (2018). Particle size distribution controls the threshold between net sediment erosion and deposition in suspended load dominated flows. *Geophysical Research Letters*, *45*(3), 1443-1452.

Falcini, F., Marini, M., Milli, S., & Moscatelli, M. (2009). An inverse problem to infer paleoflow conditions from turbidites. *Journal of Geophysical Research: Oceans*, *114*.

Fukushima, Y., Parker, G., & Pantin, H. M. (1985). Prediction of ignitive turbidity currents in scripps submarine canyon. *Marine Geology*, *67*(1), 55–81.

Garcia, M., & Parker, G. (1991). Entrainment of bed sediment into suspension. *Journal of Hydraulic Engineering*, *117*(4), 414-435.

Garcia, M., & Parker, G. (1993). Experiments on the entrainment of sediment into suspension by a dense bottom current. *Journal of Geophysical Research*, *98*(C3), 4793–4807.

Gibbs, R. J. (1974). A settling tube system for sand-size analysis. *Journal of Sedimentary Petrology*, *44*(2), 583–588.

Jameson, A., Schmidt, W., & Turkel, E. (1981). Numerical solution of the euler equations by finite volume methods using runge kutta time stepping schemes. In *14th fluid and plasma dynamics conference* (p. 1259).

Johnson, D. W. (1939). *The origin of submarine canyons: A critical review of hypotheses.* Columbia University Press.

Kostic, S., & Parker, G. (2006). The response of turbidity currents to a canyon–fan transition: Internal hydraulic jumps and depositional signatures. *Journal of Hydraulic Research*, *44*(5), 631–653. Retrieved from https://doi.org/10.1080/00221686.2006.9521713 doi: 10.1080/00221686.2006.9521713

Krizhevsky, A., Sutskever, I., & Hinton, G. E. (2012). Imagenet classification with deep convolutional neural networks. In F. Pereira, C. J. C. Burges, L. Bottou, & K. Q. Weinberger (Eds.), *Advances in neural information processing systems 25* (pp. 1097–1105). Curran Associates, Inc. Retrieved from http://papers.nips.cc/paper/4824-imagenet-classification-with-deep-convolutional-neural-networks.pdf

Kuenen, P. H., & Migliorini, C. I. (1950). Turbidity currents as a cause of graded bedding. *The Journal of Geology*, *58*(2), 91–127.

Lesshafft, L., & Marquet, O. (2010). Optimal velocity and density profiles for the onset of absolute instability in jets. *Journal of Fluid Mechanics*, *662*, 398–408.

Liang, S., & Srikant, R. (2016). Why deep neural networks for function approxima-
tion? *CoRR*, *abs/1610.04161*. Retrieved from `http://arxiv.org/abs/1610`
`.04161`

Luchi, R., Balachandar, S., Seminara, G., & Parker, G. (2018). Turbidity cur-
rents with equilibrium basal driving layers: A mechanism for long runout.
Geophysical Research Letters, *45*(3), 1518-1526. Retrieved from `https://`
`agupubs.onlinelibrary.wiley.com/doi/abs/10.1002/2017GL075608` doi:
10.1002/2017GL075608

Nakao, K., & Naruse, H. (2017, 12). Inverse analysis to reconstruct hydraulic con-
ditions of non-steady turbidity currents based on multiple grain-size classes.
EarthArXiv.

Naruse, H. (2005). Usage and advantages of an application program "stube" for set-
tling tube grain-size analysis. *Journal of the Sedimentological Society of Japan*,
62(62), 55–61.

Naruse, H., & Nakao, K. (2017, 12). Inverse analysis of turbidites by machine learn-
ing. *AGU Fall Meeting Abstracts*.

Naruse, H., & Olariu, C. (2008). Hydraulic conditions of turbidity currents es-
timated by inverse analysis. In *Fourth international conference on scour and
erosion* (pp. 591–593). Japanese Geotechnical Society.

Nielsen, M. A. (2015). *Neural networks and deep learning.* Determination Press.

Parker, G., Garcia, M., Fukushima, Y., & Yu, W. (1987). Experiments on turbidity
currents over an erodible bed. *Journal of Hydraulic Research*, *25*(1), 123–147.

Parkinson, S. D., Funke, S. W., Hill, J., Piggott, M. D., & Allison, P. A. (2017).
Application of the adjoint approach to optimise the initial conditions of a
turbidity current with the adjointturbidity 1.0 model. *Geoscientific Model
Development*, *10*(3), 1051–1068.

Paull, C. K., Talling, P. J., Maier, K. L., Parsons, D., Xu, J., Caress, D. W., . . .
Cartigny, M. J. (2018). Powerful turbidity currents driven by dense basal
layers. *Nature Communications*, *9*(1), 4114.

Pradhan, B., Lee, S., & Buchroithner, M. F. (2010). A gis-based back-propagation
neural network model and its cross-application and validation for landslide
susceptibility analyses. *Computers, Environment and Urban Systems*, *34*(3),
216–235.

Rogers, S. J., Fang, J. H., Karr, C. L., & Stanley, D. A. (1992). Determination of
lithology from well logs using a neural network. *AAPG Bulletin*, *76*(5), 731–
739.

Ruder, S. (2016). An overview of gradient descent optimization algorithms. *CoRR*,
abs/1609.04747. Retrieved from `http://arxiv.org/abs/1609.04747`

Rumble, J. R. (2018). *Crc handbook of chemistry and physics, 99th edition.* CRC
Press.

Schmidhuber, J. (2015). Deep learning in neural networks: An overview. *Neural Net-
works*, *61*, 85–117. Retrieved from `http://www.sciencedirect.com/science/`
`article/pii/S0893608014002135` doi: https://doi.org/10.1016/j.neunet.2014
.09.003

Talling, P. J., Allin, J., Armitage, D. A., Arnott, R. W. C., Cartigny, M. J. B.,
Clare, M. A., . . . Xu, J. (2015). Key future directions for research on turbidity
currents and their deposits. *Journal of Sedimentary Research*, *85*(2), 153–169.

Talling, P. J., Amy, L. A., & Wynn, R. B. (2007). New insight into the evolution of
large-volume turbidity currents: Comparison of turbidite shape and previous
modelling results. *Sedimentology*, *54*(4), 737–769.

Talling, P. J., Masson, D. G., Sumner, E. J., & Malgesini, G. (2012). Subaqueous
sediment density flows: Depositional processes and deposit types. *Sedimentol-
ogy*, *59*(7), 1937–2003.

Vangriesheim, A., Khripounoff, A., & Crassous, P. (2009). Turbidity events observed
in situ along the congo submarine channel. *Deep Sea Research Part II: Topical*

Studies in Oceanography, *56*(23), 2208–2222.

Wang, Z., & Bovik, A. C. (2009). Mean squared error: Love it or leave it? a new look at signal fidelity measures. *IEEE Signal Processing Magazine*, *26*(1), 98–117. doi: 10.1109/MSP.2008.930649

Weimer, P., & Slatt, R. M. (2007). Introduction to the petroleum geology of deepwater settings. *AAPG Studies in Geology*, *57*, 149-227.

Wright, S., & Parker, G. (2004). Flow resistance and suspended load in sand-bed rivers: Simplified stratification model. *Journal of Hydraulic Engineering*, *130*(8), 796–805.

Xu, J. P., Noble, M. A., & Rosenfeld, L. K. (2004). In-situ measurements of velocity structure within turbidity currents. *Geophysical Research Letters*, *31*(9).

Yabe, T., Xiao, F., & Utsumi, T. (2001). The constrained interpolation profile method for multiphase analysis. *Journal of Computational Physics*, *169*(2), 556–593.